DESIGN OF A CONTINUOUS FLOW MAGNETIC RESONANCE SYSTEM FOR RHEOLOGICAL CHARACTERIZATION

A THESIS SUBMITTED TO
THE GRADUATE SCHOOL OF NATURAL AND APPLIED SCIENCES
OF
MIDDLE EAST TECHNICAL UNIVERSITY

BY

ZİKRULLAH BÖLÜKKAYA

IN PARTIAL FULFILLMENT OF THE REQUIREMENTS
FOR
THE DEGREE OF MASTER OF SCIENCE
IN
FOOD ENGINEERING

DECEMBER 2022

Approval of the thesis:

DESIGN OF A CONTINUOUS FLOW MAGNETIC RESONANCE SYSTEM FOR RHEOLOGICAL CHARACTERIZATION

submitted by **ZİKRULLAH BÖLÜKKAYA** in partial fulfillment of the requirements for the degree of **Master of Science** i**n Food Engineering, Middle East Technical University** by,

Prof. Dr. Halil Kalıpçılar
Dean, Graduate School of **Natural and Applied Sciences** _____

Prof. Dr. Hami Alpas
Head of the Department, **Food Engineering** _____

Assoc. Prof. Dr. Mecit Halil Öztop
Supervisor, **Food Engineering, METU** _____

Prof. Dr. Behiç Mert
Co-Supervisor, **Food Engineering, METU** _____

Examining Committee Members:

Prof. Dr. Hami Alpas
Food Engineering, METU _____

Assoc. Prof. Dr. Mecit Halil Öztop
Food Engineering, METU _____

Prof. Dr. Behiç Mert
Food Engineering, METU _____

Prof. Dr. Deniz Çekmecelioğlu
Food Engineering, METU _____

Assoc. Prof. Dr. Evrim Umut
Vocational School of Health Services, Dokuz Eylul University _____

Date: 02.12.2022

I hereby declare that all information in this document has been obtained and presented in accordance with academic rules and ethical conduct. I also declare that, as required by these rules and conduct, I have fully cited and referenced all material and results that are not original to this work.

Name Last name: Zikrullah Bölükkaya

Signature:

ABSTRACT

DESIGN OF A CONTINUOUS FLOW MAGNETIC RESONANCE SYSTEM FOR RHEOLOGICAL CHARACTERIZATION

Bölükkaya, Zikrullah
Master of Science, Food Engineering
Supervisor: Assoc. Prof. Dr. Mecit Halil Öztop
Co-Supervisor: Prof. Dr. Behiç Mert

December 2022, 91 pages

In food processing, handling, pumping, and extrusion of dilute and viscous fluids, emulsions, and suspensions are important for production purposes. Magnetic Resonance Imaging (MRI) offers the possibility to measure the rheological properties of different fluids in a non-invasive mode and is highly selective (in situ, online) to study the structural changes, or inner transport processes (without wasting samples and disturbing production) in flowing materials. In this study, a bench top Magnetic Resonance Imaging system operating at a frequency of 24.15 MHz (~0.50 T), equipped with a radio frequency coil of 10mm was converted to a flow-MR system or the so-called MR-Viscometer to measure the rheological constants of different Newtonian and Non-Newtonian fluids. At the first step, mechanical energy calculations were made to determine the system dimensions, and fittings and to integrate the pressure transducer of the system. Since a peristaltic pump was used there was the ‘pulsation’ problem, which could have caused problems in the MR velocity images was observed. Thus, a dampener was added to the system by making the proper calculations. Once the design calculations were complete and the system

was set up, experimental trials were carried out to test the system. Almond milk and whole milk were tested at different pump flow rates to check whether the system was operating properly. Almond milk was a shear-thinning fluid (K=0.0254 Pa.s, n =0.783) whereas whole milk was Newtonian (μ=0.0032 Pa.s). The error between theoretical and experimental pressure differences was found to be 31-40% for whole milk and 23-45% for almond milk. It was interesting to observe that at different flow rates there was a significant and positive correlation ($r=0.99$, $p<0.05$) between the experimental and theoretical pressure differences which indicated that there was an '**inherent'** error associated with the pressure measurements. Error rates of whole milk higher at low flow rates were explained by the high slip velocities and the high error at high flow rates for almond milk was explained with dampener problems. Measurements were also conducted with methylcellulose solutions and rheological constants were compared with the conventional rheometer experiments. 'n' values were not found to be different for the flow MR and conventional measurements ($p>0.05$) whereas K values were significantly higher in flow MR results. However, despite the K values higher in flow MR results, there was a positive and significant correlation ($p<0.05$) between the two measurements confirming that the system was working properly but the pressure measurement error needs to be corrected to get an equal number from both methods.

Keywords: Benchtop magnetic resonance imaging (MRI); flow; velocity profile; rheology

ÖZ

REOLOJİK KARAKTERİZASYON İÇİN SÜREKLİ AKIŞLI MANYETİK REZONANS SİSTEMİ TASARIMI

Bölükkaya, Zikrullah
Yüksek Lisans, Gıda Mühendisliği
Tez Yöneticisi: Doç. Dr. Mecit Halil Öztop
Ortak Tez Yöneticisi: Prof. Dr. Behiç Mert

Aralık 2022, 91 sayfa

Gıda proses mühendisliğinde, seyreltik ve viskoz sıvıların, emülsiyonların süspansiyonların taşınması, pompalanması, ekstrüzyonu, üretim açısından önemlidir. Manyetik Rezonans Görüntüleme (MRI), farklı sıvıların reolojik özelliklerini tahribatsız bir modda ölçme olanağı sağlayan ve akıştaki yapısal değişiklikleri veya iç taşıma süreçlerini ön hazırlık gerektirmeden sunan bir tekniktir. Bu çalışmada, 24.15 MHz (~0,50 T) frekansında çalışan ve 10 mm'lik bir radyo frekans bobini ile donatılmış bir masa üstü Manyetik Rezonans Görüntüleme sistemi, bir akış-MR sistemine veya diğer bir adla MR-Viskozimetre'ye dönüştürülmüş ve Newtonian/Newtonian olmayan akışkanların reolojik sabitleri hesaplanmıştır. İlk adım olarak sistem ölçülerinin, bağlantı elemanlarının belirlenmesi ve sisteme basınç transdüserinin entegre edilmesi için mekanik enerji hesapları yapılmıştır. Sistemde peristatik pompa kullanılmasına karar verildiğinden, MR hız görüntülerinde 'darbe' sorunu ile karşılaşılmıştır. Bu nedenle uygun hesaplamalar yapılarak sisteme darbe sönümleyici eklenmiştir. Tasarım hesaplamaları tamamlandıktan ve sistem kurulduktan sonra, sistemi test etmek için deneysel denemeler yapılmıştır. Badem sütü ve tam yağlı süt, sistemin düzgün çalışıp çalışmadığını kontrol etmek için farklı pompa akış hızlarında test edilmiştir. Badem sütü kayma inceltici bir sıvı iken

(K=0.0254 Pa.s, n =0.783), tam yağlı süt beklendiği üzere Newtonian özellik göstermiştir (μ=0.0032 Pa. s). Teorik ve deneysel basınç farkları arasındaki hata tam yağlı süt için %31-40, badem sütü için %23-45 arasında bulunmuştur. Farklı akış hızlarında deneysel ve teorik basınç farkları arasında anlamlı ve pozitif bir korelasyon ($r=0.99$, $p<0.05$) olduğu gözlenmiştir. Bu durum basınç ölçümleriyle ilişkili 'doğal' bir hata olduğunu göstermiştir. Düşük debilerde tam yağlı sütün hata oranlarının daha yüksek olması duvardaki kayma hızlarının yüksek olması, badem sütünde yüksek debilerde hatanın yüksek olması ise darbe sönümleyicisindeki yüksek basınç ile açıklanmıştır. Metil selüloz çözeltileri ile de ölçümler yapılmış ve reolojik sabitler geleneksel reometre deneyleriyle karşılaştırılmıştır. Akış MR ve konvansiyonel ölçümler için '*n*' değerleri farklı bulunmazken ($p>0,05$), akış MR sonuçlarında K değerleri anlamlı derecede yüksek bulunmuştur ($p<0,05$). Akış MR sonuçlarında K değerleri daha yüksek olmasına rağmen 2 ölçüm arasında pozitif ve anlamlı bir korelasyon ($p<0.05$) olması sistemin düzgün çalıştığını ancak basınç ölçüm hatasının düzeltilmesi gerektiğini doğrulamaktadır.

Anahtar Kelimeler: Masaüstü Nükleer Manyetik Rezonans Görüntüleme; Sürekli Akış MRG; TD NMR;Akış; Reoloji

To best of bests, my beloved family…

ACKNOWLEDGMENTS

I'd like to express my gratitude to Assoc. Prof. Dr. Mecit Halil Öztop for his always support, patience, advice, and encouragement. I have felt lucky to be in his team because he has encouraged me to use my interests and skills fully. He's always been more than an advisor to me. Thanks to him, I had memorable experiences, which have changed my perspective and life in a good way. I'd also like to thank my co-advisor Behiç Mert for his valuable suggestions and comments. I'd like to express my big thanks to Prof. Michael J. McCarthy. He answered my questions and helped me to solve the problems with his genuine help and expertise.

I'd like to offer my deepest thanks to my lab friends (Gözde Özeşme Taylan, Eren Cantürk, Eren Başdemir, Esra Nur Kaya, Şirvan Sultan Uğuz, Sultan Kurt, Sena Kuzu, and Tayfun Şener) and research assistants Esmanur İlhan, Kübra Ertan, and Selen Güner, for being so nice, encouraging and support. Time that I have with them means a lot to me. Although I am in low mood, they realize it and they help me to positive and control the situation. Some of the rituals will stay in mind that morning and evening walk to/from the lab. On the way, we watch small field mice while we are afraid of any voice of dog.

I'd like to give a big hug to my family. My parents don't even understand what graduate school means but they support me to chase my dream. My sisters and me have always been with me and they are also friends to me. I love you all.

I also would like to say thank OztopLab family. OztopLab family includes many great people and share great experience in the same roof. There are many more valuable people in the lab I couldn't stop listing.

I'd like to express my deepest gratitude to Mook Kornkanok Ketbumrung. Despite to great distance, she has always been the closest one to me, always supportive and helpful. Lastly, this work is funded by The Scientific and Technological Research Council of Turkey (TUBİTAK) with project number 121O091.

TABLE OF CONTENTS

LIST OF TABLES

TABLES

LIST OF FIGURES

FIGURES

CHAPTER 1

INTRODUCTION

1.1 Magnetic Resonance Imaging (MRI)

The employment of radiofrequency range pulses to obtain information on the internal architecture of human tissues gave rise to the magnetic resonance imaging (MRI) method, which has been traditionally employed in medical applications to analyze the structure of soft tissue as a tool for clinical diagnosis. However, because of its precision and adaptability, MRI has demonstrated to be a powerful analytical tool for engineering study as well (Kirtil & Oztop, 2016b).

The signal acquired in MRI is obtained through the action of the radiofrequency (RF) pulses. RF waves is a type of the electromagnetic waves as seen in Figure 1.1. The radio frequency spectrum contains a set of frequencies of the electromagnetic spectrum including radiofrequencies (RF) extending from 30 kHz to 300 GHz, which includes MRI in between 1 to 100 MHz. In order to understand how signal is generated in NMR, it is important to understand some of the basic concepts.

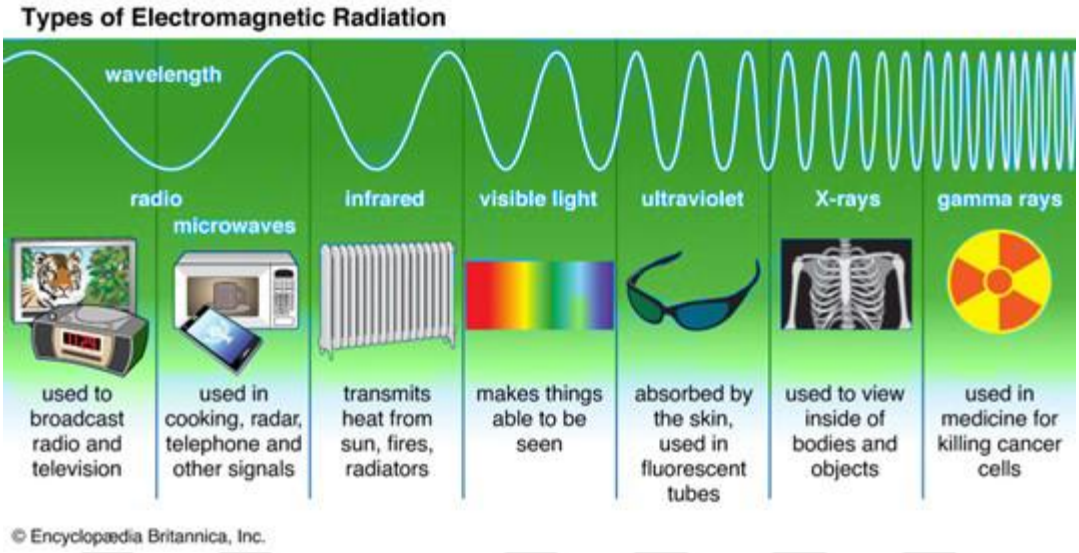

Figure 1-1. Electromagnetic spectrum (The Editors of Encyclopedia Britannica, 2022)

1.1.1 Nuclear Spins and Precession

Nuclear spin refers to the magnetic characteristics of hydrogen atoms (protons) (Figure 1.2). These spins, which are represented by vectors, behave like small revolving magnets. Net magnetization is the total of all the tiny magnetic fields of each spin. These vectors' directions are often distributed at random. The result is a null net magnetization when all the spins are added together. Nuclear spins align with the external field in the presence of a strong external magnetic field (referred to as B0). Some of the spins are parallel to the field while others are antiparallel to the field (anti-parallel).

Figure 1-2. Nuclear spin

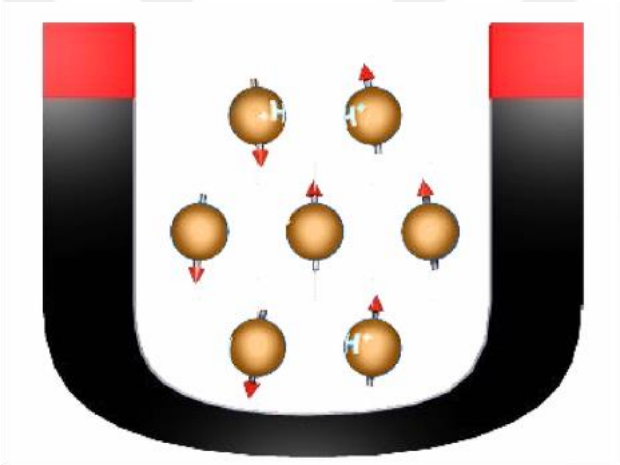

Figure 1-3. Alignment of spins with magnetic field

Not often do the protons face the external magnetic field directly. Instead, they create a motion known as precession that resembles a spin top, shown in Figure 1.4.

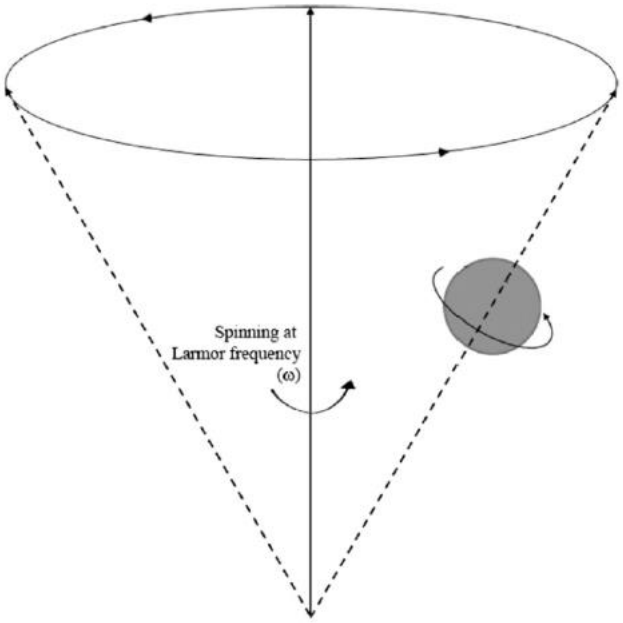

Figure 1-4. Schematic depicting the precessional motion of protons

The following relation explained with the frequency of this circular motion (Griffiths, 1997) ;

$\boldsymbol{\omega = \gamma B_o}$ where;

- ω = angular precessional frequency of proton,
- γ = gyromagnetic ratio and
- B_0 = strength of the external magnetic field.

1.1.2 Signal Acquisition

When the longitudinal magnetization is disturbed by a RF pulse of the same frequency, the system becomes '*on resonance*' and magnetization is flipped to the xy plane.

The electromagnetic RF pulse only affects protons whose spin frequency is the same as the electromagnetic RF pulse. Excitation is the alteration of the spin-equilibrium state and the electromagnetic energy absorption by atomic nuclei (Griffiths, 1997). When the system returns from this state of imbalance to equilibrium (*relaxation*), electromagnetic energy is emitted. Excitation modifies energy levels and spin phases. A single proton goes to a higher energy state at the quantum level (from parallel to anti-parallel). A spiral movement down to the XY plane is the result on the macroscopic net magnetization vector (Gladden & Sederman, 2017).

The net magnetization vector can be divided into two parts: a transverse part that is on the XY plane and a longitudinal part that runs along the Z axis and is aligned with B0.

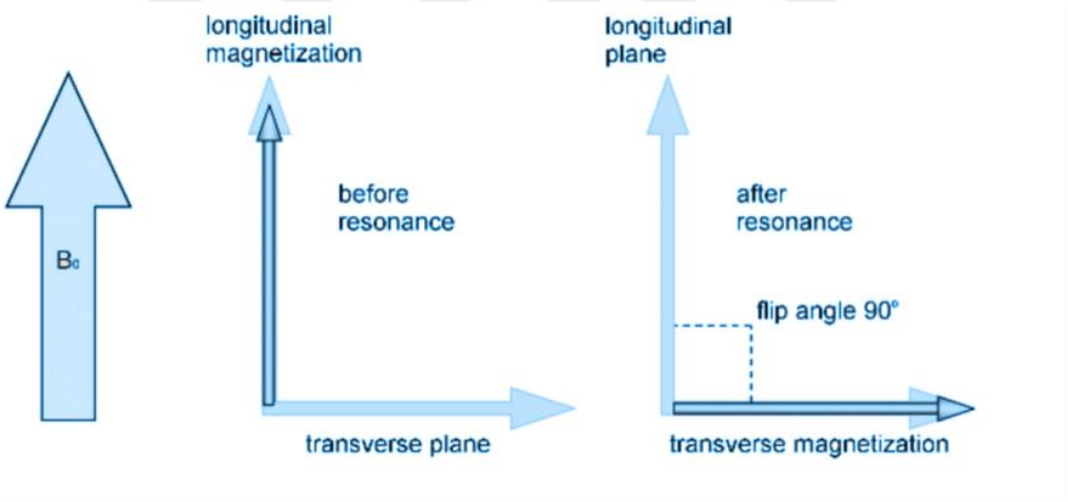

Figure 1-5. Schematic representation of the longitudinal/transverse magnetization (Westbrook & Talbot, 2018)

With the exception of a 180° flip angle, longitudinal magnetization diminishes during excitation and a transverse magnetization emerges. Recovery rate of longitudinal magnetization is described as T1 (spin- lattice) relaxation time, whereas

decay of transverse magnetization is known as T2 (spin-spin) relaxation time. The disparity between the number of spins in parallel and anti-parallel states is what causes longitudinal magnetization. Spins entering phase coherence is what causes transverse magnetization.

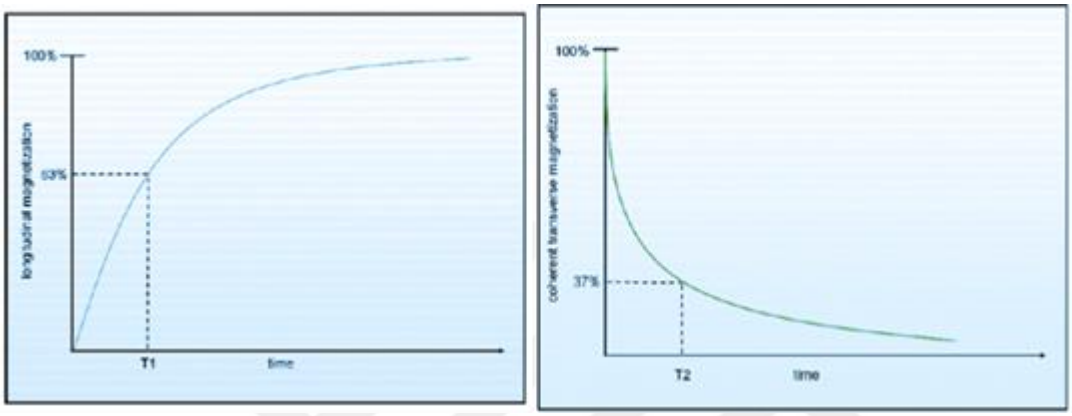

Figure 1-6. Longitudinal and transverse relaxation curves

An overview of the signal acquisition is also summarized in Figure 1.7.

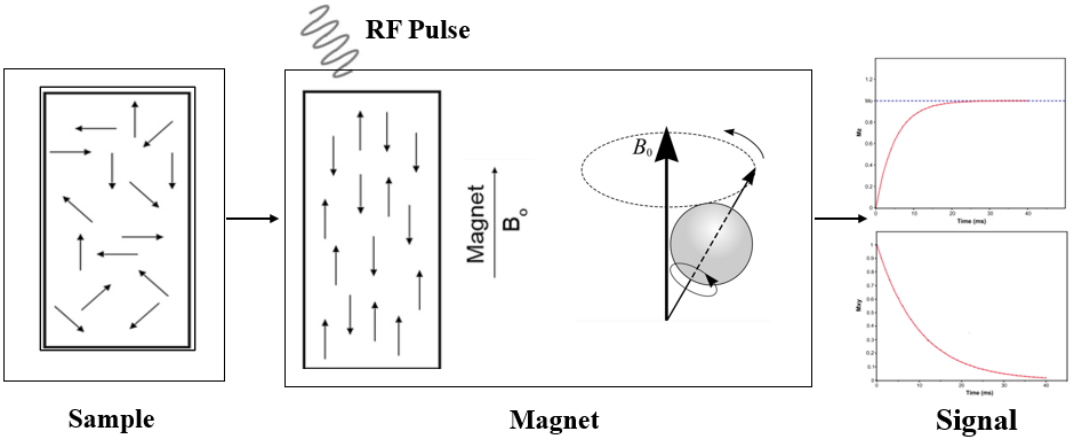

Figure 1-7. Schematic representation of acquiring signal from a sample

1.1.3 Image Acquisition

The simple NMR signal obtained with the RF pulse, T_1 recovery and T_2 relaxation give information from the sample as a whole and do not provide spatial information. To assign a position to the various signals in imaging, spatial data must be added to the signal. Gradients are used to encode the NMR signal's spatial information. Gradients are essentially wire loops or thin conductive sheets mounted on a cylinder that is just inside the bore of an MRI scanner (Harmonay, 2018). Whenever an electrical current flows through these coils, a secondary magnetic field is created. The main magnetic field is slightly but predictably distorted by this gradient field. The primary purpose of a gradient coil is to predictably regulate the main magnetic field in space, changing the spins' Larmor frequencies according to their positions (Winkler et al., 2018). Thus, enabling spatial encoding of the MR signal. A simple representation of the gradients is shown in Figure 1.8.

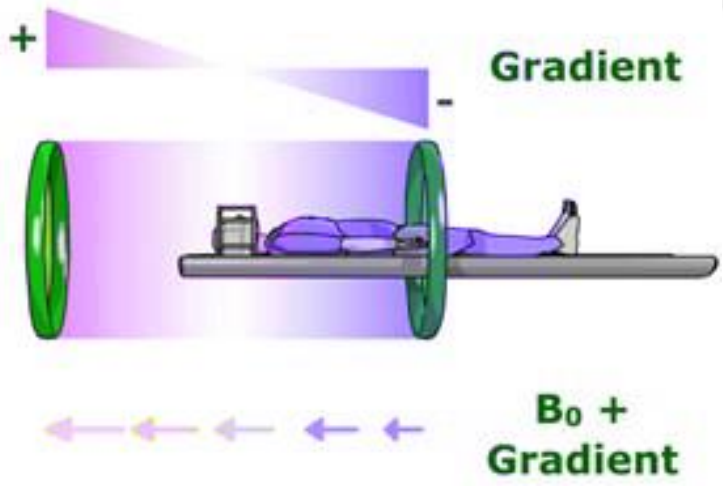

Figure 1-8. Representation of a gradient in an MRI system (IMAIOS, 2019)

Spatial encoding is based on application of different magnetic field gradients to a sample. The volume of interest is first chosen using a slice selection gradient (SSG). The position of each point within this volume is then encoded vertically,

horizontally, and using a phase encoding gradient (PEG) and a frequency encoding gradient, respectively (FEG). Although the various gradients used for spatial localization have the same characteristics, they are applied at various points and in various directions.

Slices can be chosen on any spatial plane because of gradient equivalence in all three spatial dimensions; *axial*, *sagittal*, *coronal*.

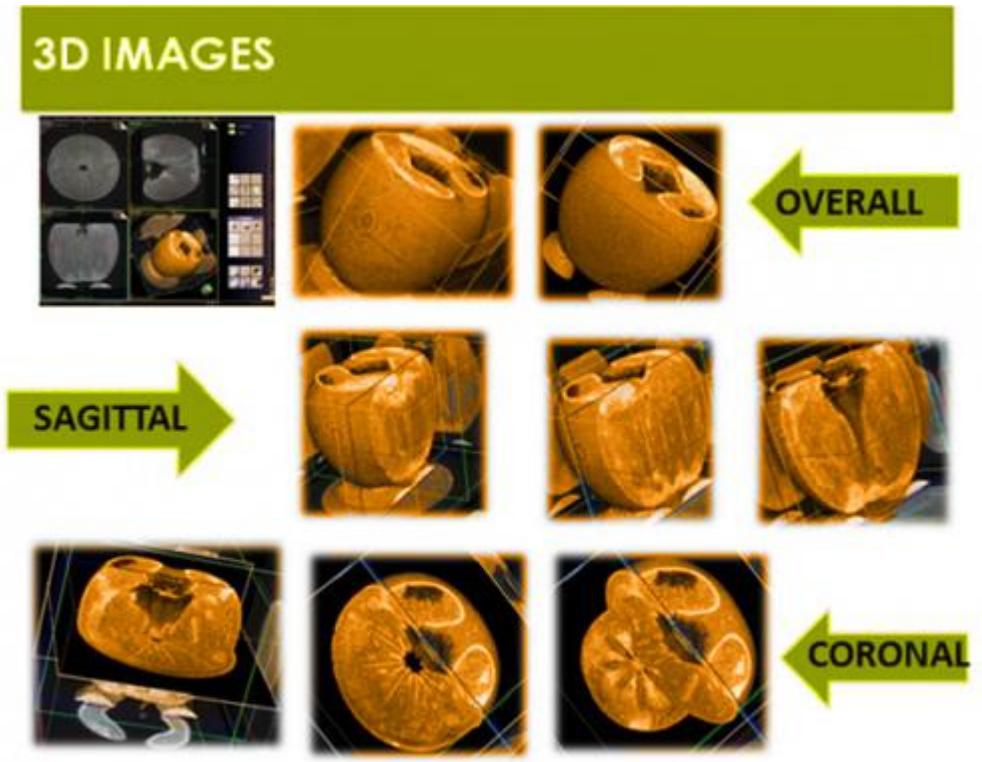

Figure 1-9. Representative imaging planes for persimmon fruit

An image is acquired by applying; 90, 180^{o} pulses and by applying gradients within the MRI system. The coherent application of the pulses and the gradients are known

as a pulse sequence and the simple and most commonly used pulse sequence is the Spin Echo sequence (SE).

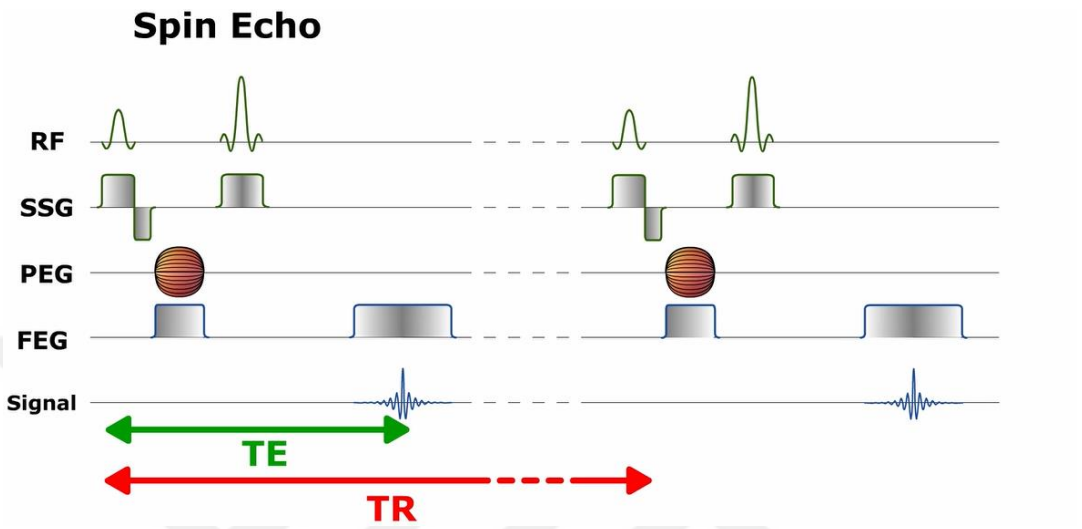

Figure 1-10. Summary of the spin echo (SE) sequence

1.1.3.1 Slice Selection Gradients (SSG)

The first step of spatial encoding is selection of a slice. To do this, the Slice Selection Gradient (SSG), a magnetic field gradient, is applied perpendicular to the chosen slice plane. The protons' resonance frequency varies in proportion to SSG when this is added to B0 (Larmor equation). The frequency of the protons in the chosen slice plane is the same as the frequency of the RF pulse that is simultaneously applied. Only the protons on this plane experience a change in their magnetism as a result. The hydrogen nuclei outside the slice plane are not excited, hence they won't provide a signal. The term "selective pulse" refers to the RF pulse that is connected to the slice selection gradient and the modified resonance frequency. The magnetic field gradients will once more trigger these protons in the slice plane to encode their position in both the horizontal and vertical directions (Hashemi et al., 2010).

An RF pulse does not have single frequency alone since, it covers a certain bandwidth, which depends on the shape and duration of the pulse. In order to change the slice thickness either the bandwidth or the gradient strength should be changed (IMAIOS, 2019):

$$Slice\ thickness = \frac{Bandwidth}{\gamma . SS_g} \qquad (1.1)$$

- *By varying the selective pulse's bandwidth and the slice selection gradient's amplitude, the thickness of the slice can be changed*
- *The broader the bandwidth, the more protons are stimulated, and the thicker the slice are for a fixed amplitude gradient*
- *The larger the gradient, the greater the fluctuation of precession frequency in space, and the thinner the slice are true for a fixed bandwidth*

As seen in Figure 1.10, SSG is applied during the pulses and after 90^o in negative direction. Due to the resulting dispersion in the resonance frequency, the SSG will experience spin dephasing in the case of an RF pulse at an angle lower than 180 degrees. To counteract this effect, a second gradient lobe is applied immediately after the selective RF pulse (concomitant with the gradient), along the same axis but in the opposite direction, and with a surface (amplitude x time) equal to half that of the first gradient lobe. Since the dephasing effects in the case of a 180° pulse neutralize symmetrically with regard to the RF pulse's center, no rephasing lobe is necessary. On the other hand, Since the slice profile is not ideal, a 180° rephasing pulse that simply inverts the stimulated spins' magnetization will also create a shift in the undesirable spins at the slice's edge (IMAIOS, 2019). On either side of the 180° pulse, two identical gradient lobes can be inserted to prevent this problem:

- *These lobes will have an equal impact on the magnetic field before and after the 180-degree pulse and will cancel each other out*

- *The second additional gradient lobe will have the opposite effect of the 180° pulse, canceling off the magnetization near the edge of the slice*.

1.1.3.2 Phase Encoding Gradients (PEG)

The 2nd step in spatial encoding is to apply a phase encoding gradient which is usually applied in the vertical direction. The phase encoding gradient (PEG) is applied for a limited time period. It alters the spin resonance frequencies as it is being applied, causing dephasing that lasts even after the gradient is stopped. All of the protons as a result precess in various phases but at the same frequency. The same phase will be shared by all of the protons in a row that is parallel to the gradient direction. Up until the signal is recorded, this phase difference is present. Each row of protons will be slightly out of phase when the signal is received. This is equivalent to their signals being slightly out of phase (Westbrook & Talbot, 2018). The gradient is used with distinct, routinely incremented values to carry out the various phase encoding stages. It is bipolar, which means that positive and negative values that are symmetrical to 0 are employed as gradients.

The several, regularly incremented dephased acquisitions must be multiplied in order to produce an image. We perform « n » acquisitions with a distinct phase encoding gradient for a spin echo sequence with « n » rows.

1.1.3.3 Frequency Encoding Gradients (FEG)

Setting a frequency encoding gradient when the signal is received completes the spatial encoding process. Throughout the time it is applied, this alters the Larmor frequencies in the horizontal direction. As a result, it generates proton columns that are all the same Larmor frequency. The frequency data are provided as this gradient is applied instantly upon receiving the signal (Hashemi et al., 2010).

1.1.3.4 Duration of an Imaging Experiment

The main parameter that determines the duration of the imaging are listed as following:

- ***TR*** *= Repetition time (the time until the application of the second 90^o pulse from the beginning)*
- $\boldsymbol{N_p}$ *= Number of phase encoding steps*
- $\boldsymbol{N_{ex}}$*= Number of excitations (number of times that the spin echo sequence is repeated)*

Duration is represented as:

$$Duration = TR * Np * Nex \qquad (1.2)$$

1.1.3.5 Summary of the Imaging Gradients

Each gradient has a unique strength (a higher or lesser fluctuation in the field for a given unit of distance), direction, and moment and time of application (Bernstein et al., 2004).

- *The protons' precession frequency is altered by the slice selection gradient, causing them to shift in response to an RF pulse of the same frequency*
- *All of the RF pulses are concurrently subjected to* ***the slice selection gradient****.*
- *Slice thickness and profile are determined by RF pulse bandwidth and waveform.*
- *Each* ***phase encoding step*** *functions as a sort of sieve, enabling horizontal signals with uniform spacing.*
- *Without phase encoding, the signal will originate from the entire slice.*
- *For this reason, it takes several phases of phase encoding to gather enough information to rebuild the image.*

- *An image can be recreated by evaluating the signals obtained with a large number of distinct profiles, or fine combs.*
- *The signal is digitalized at regular time intervals when* ***frequency-encoding gradient*** *is used.*
- *Every signal sample is equivalent to a specific accumulation of the gradient impact on the entire splice signal: the longer the period, the longer the gradient effect on the spins, and the bigger their phase alteration.*
- *While phase spatial encoding requires repeating the imaging process, frequency spatial encoding simply requires a few milliseconds of signal reading. A single-phase encoding step is carried out throughout each repetition period (TR) in a traditional spin echo sequence. Phase encoding takes substantially longer to complete than frequency encoding since TR values can last up to 3 seconds.*
- *An image of the slice plane is created by processing all the signals from the same slice after they have been captured in k-space.*

1.1.4 Image Construction

A mixture of RF pulses with varying amplitudes, frequencies, and phases that carry spatial information make up the signal obtained from an MR signal. Raw data from this signal are converted to digital form and written into the **k-space** data matrix. Use of a *2D inverse Fourier Transform* is required to convert k-space data to a picture. The spatial frequency information of an object in two or three dimensions is represented by the k-space. The area covered by the phase and frequency encoding data serves as the definition of the k-space (Moratal et al., 2008).

To understand *k* space better, let us first look at very simply the Fourier Transform which is the most important mathematical transformation that is used in MRI (Figure 1.11). An MR signal can be divided using the Fourier transform, a

mathematical method, into a collection of sine waves with various frequencies, phases, and amplitudes. Since spatial encoding in MR imaging involves frequencies and phases, it is best analyzed by Fourier techniques (Bracewell R, 1986).

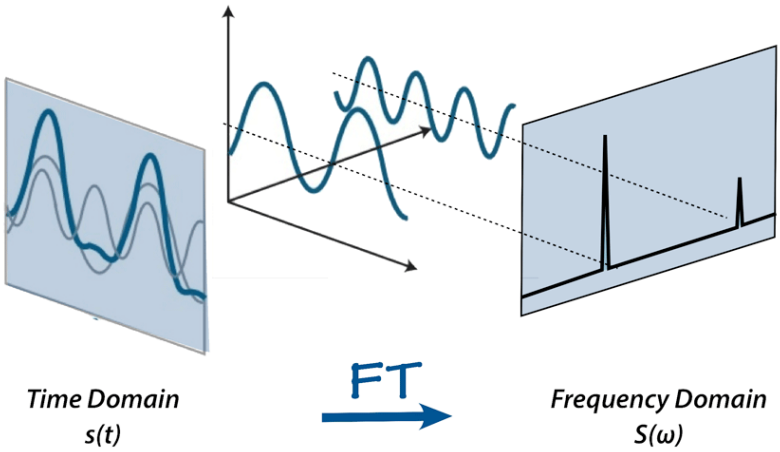

Figure 1-11. Basic representation of FT

Fourier transformation is the mathematical procedure connecting s(t) and S(ω). If s(t) is specified, S(ω) may be computed, and vice versa.

Fourier Transform: $S(\omega) = \int_{-\infty}^{\infty} s(t)e^{-i\omega t}dt$ (1.3)

Inverse Fourier Transform: $s(t) = \frac{1}{2\pi}\int_{-\infty}^{\infty} S(\omega)e^{i\omega t}d\omega$ (1.4)

Every "star" in k-space represents a data point that was obtained from the MR signal (Figure 1.12). Each star's brightness indicates how much of its particular spatial frequency contributed to the final image (Moratal et al., 2008). k-space cells are often shown on a rectangular grid with the primary axes k_x and k_y. The image's x- and y-

axes are represented by the k_x and k_y axes of k-space, respectively. The k-axes, however, represent spatial frequencies in the x- and y-directions rather than positions. Individual pixels (x, y) in the image do not match up exactly with individual points (k_x, k_y) in k-space. The spatial frequency and phase data for each pixel in the final image are contained in each k-space point. On the other hand, every pixel in the image maps to each and every point in k-space (Hashemi et al., 2010). The k-space representation of the MR image is very similar diffraction patterns generated by *x-ray crystallography*, *optics*, or *holography*.

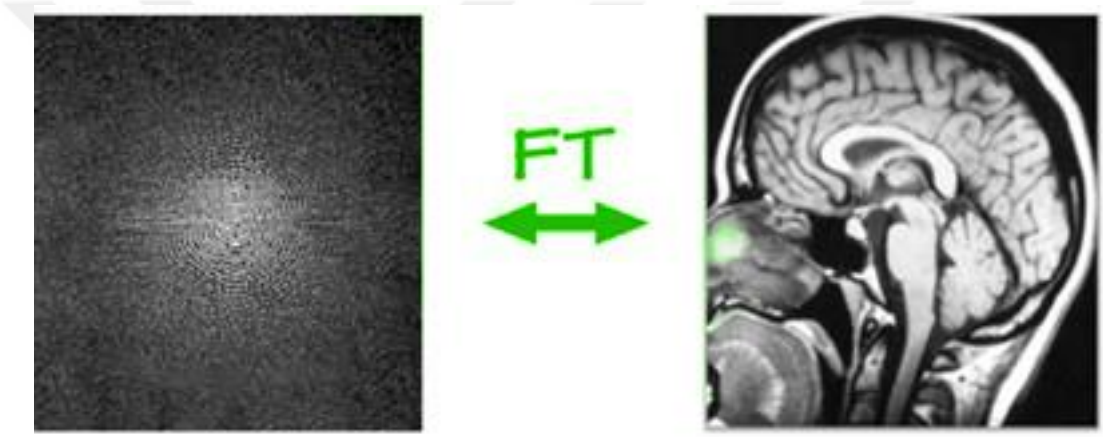

Figure 1-12. k-space is the Fourier transform of the MR image (Moratal et al., 2008)

1.1.5 Flow Imaging

Conventional rheological measurements may not be sufficient to obtain detailed information about the flow field generated by the device that are used to induce deformational flow. In addition, visualizing, in real time, strain-rate heterogeneity and discontinuity, fracture and wall slip may not be possible (Callaghan, 2006). While optical methods, such as laser *Doppler velocimetry*(Shapley et al., 2004) or *ultrasound velocimetry* (Manneville et al., 2004), can be highly effective flow visualization tools, they both require scattering from refractive index or density heterogeneity and they both suffer from some limitation in the available geometry.

In the case of light scattering applications, optical transparency requirements are the main limiting factors. In contrast, NMR velocimetry (Callaghan, 2006, 2012; Callaghan et al., 1988) suffers no transparency constraints and full three-dimensional velocity fields may be determined in any geometry whatsoever.

Nuclear Magnetic Resonance (NMR) provides the opportunity to conduct measurements in situ and online that are non-invasive, non-destructive, and highly selective in order to examine the structure, structural changes, or inner transport processes in flowing materials without the need for preparations (Götz & Zick, 2008). Use of NMR for rheological characterization is also known as Rheo-NMR (Callaghan, 2006, 2012; Götz & Zick, 2008). All NMR applications including flow behavior, flow-induced structural changes, and NMR data are collectively referred to as rheo-NMR. Rheo-NMR enables;

-to conduct flow experiments (viscometric flows: tube flow, Couette flow, plane shear flow, plate/plate, cone/plate) in NMR devices to determine the corresponding velocity profiles (Giitz et al., 1994; Pope & Yao, 1993)*; to derive the corresponding viscosity- and wall slip functions; to study and quantify flow induced structural changes by means of appropriate NMR experiments* (Callaghan, 1999; Nakatani et al., 1990; Xia & Callaghan, 1991)*; to arrive at correlations between macroscopic rheological material characteristics and microscopic NMR data. By using an online determination of practice-relevant values, these correlations could be very beneficial for an efficient process and quality control (viscosity, molar mass)*.

Velocity imaging by MRI could be performed using different approaches. Three categories of flow imaging techniques exist (Pope & Yao, 1993):

- *Using **inflow/outflow techniques**, track alterations in signal strength brought on by spins moving into or out of the chosen slice;*

- *By frequency encoding the displacements of the various velocity components during the imaging sequence,* ***time-of-flight*** *algorithms may distinguish between them*
- ***Phase-encoding techniques*** *use flow-dependent phase shifts to directly communicate velocity information*

In this study, phase encoding methods have been used to obtain velocity image. Pulsed gradient spin-echo (PGSE) pulse sequence is most commonly used for that purpose (Arola, Barrall, Powell, Mccarthy, et al., 1997; Callaghan, 1999, 2006, 2012; Xia & Callaghan, 1991). In PGSE sequence, using an applied G gradient and a 90^o radio-frequency (RF) pulse, spins in a plane perpendicular to the flow direction are excited. After excitation, the first G, gradient pulse causes a spatially dependent phase shift in the spins, which is then reversed by a 180^o RF pulse. The second G, gradient imposes a net phase proportional to the final position. The net phase is proportional to the distance traveled during the time interval, T. Applying a gradient upon signal acquisition, G_x or G_y yields position-dependent displacement measurements (Arola, Barrall, Powell, Mccarthy, et al., 1997). A typical velocity image is shown in Figure 1.13. In order to have a proper velocity image; flow should be in laminar region and pump should pump the fluid without pulsation. The other important requirement is the 'shear rate' range. Depending on the *flow rate*; a preliminary 'shear' rate information should be provided to the system so that velocity sweep width could be adjusted. Velocity sweep with is directly related with the encoding range in the image. If not set properly, velocity is wrapped in the image and image quality is affected adversely.

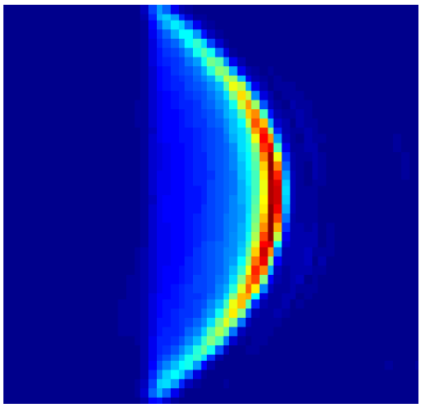

Figure 1-13. A typical velocity image

Once the image is obtained; velocity profile is set to a 3rd or 4th order polynomial (Choi et al., 2005; Tozzi et al., 2014). A set of shear rates $\dot{\boldsymbol{\gamma}}(\mathbf{r})$ is obtained by differentiation of the velocity profile. The corresponding shear stresses are computed as a function of the radius as $\tau(r) = \frac{\Delta P r}{2L}$ where $\frac{\Delta P}{L}$ is the pressure drop per unit length (*L is the length of the pipe*). Using, shear stress/shear rate data, viscosity or non-Newtonian constants are calculated.

When the fluid has a yield stress, velocity also shows a difference. In Figure 1.14, a velocity image of a delignified cellulose solution is given.

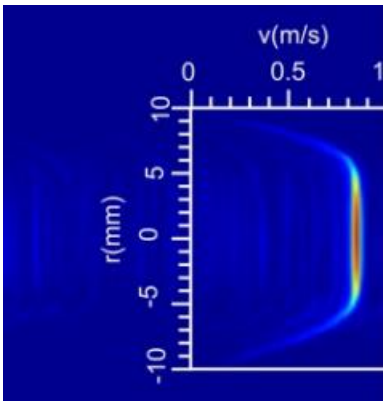

Figure 1-14. Velocity image of a fluid with yield stress (Lavenson et al., 2011)

The presence of a yield stress in the flowing material is implied by a velocity profile with zero velocity gradient. In such a flow, the suspension travels as an unyielding "plug" of material. The velocity profile is fitted to the expected value using a Herschel-Bulkley rheological model to get the plug radius (de Freitas Maciel et al., 2013). To calculate the yield stress, the plug radius and pressure drop are combined (Lavenson et al., 2011).

$$\sigma_o = \frac{\Delta P R_{plug}}{2L} \qquad (1.5)$$

Yoghurt (Yoon & McCarthy, 2002), carboxymethyl cellulose (Arola, Barrall, Powell, Mccarthy, et al., 1997), low density polyethylene melt (Uludag et al., 2001), chocolate melt (Wichchukit et al., 2006), tomato concentrates (Lee et al., 2002) have all been evaluated by MRI systems. But none of those studies utilized a bench top MRI system integrated with a small peristatic pump.

In this study, a flow assisted MRI system was designed mechanically and later almond milk, whole milk, methylcellulose solutions were tested for rheological characterization of different fluids.

1.1.6 Objective of the Study

In this thesis, the goal is to convert a bench top MRI system to an MR Rheometer to investigate the flow behavior of different fluids nondestructively, in continuous mode. Under this goal, the specific objectives of the thesis are defined as follows;

- *Design the hardware of the flow system by engineering design calculations;*
- *Integrate a peristaltic pump to the system so that the system could later be used for systems like 'digestion simulation' and solve the 'pulsation' problem of the peristaltic pump using engineering approaches;*
- *Test the system on Newtonian/Non-newtonian fluids to obtain velocity images and test the parameters to improve the signal to noise ratio of the velocity images;*
- *Calculate rheological constants from the velocity profiles and compare the results with conventional rheometer results.*

CHAPTER 2

MATERIALS AND METHODS

In this thesis; an MR-assisted continuous flow system for rheological characterization of Newtonian/Non-Newtonian fluids was designed from basics and run for rheological measurements.

A flow system has been integrated into a benchtop MR system to let the acquisition of a flow image which was further used for rheological characterization. Teflon tubing, T pipes, elbows, pressure transducers, and a peristaltic pump were used to construct the system as described later.

Two pressure transducers were used (Model, DMS300, IMENS Control Technologies, Istanbul, Turkiye) to record the inlet and outlet pressure to the radio frequency coil. A data transmitter (LabJack T7i, California, USA) was used to connect pressure sensors to the software. A MATLAB code was created to convert the LabJack output of the the transducers to pressure values. The specifications of the transducers were used to convert the voltage to pressure values. Pressure transducers report an average of the 20 readings as an input to flow image acqusitions. The code is available in Appendix B.2.

2.1 Engineering Design

2.1.1 Draft Design

As the 1st step, a draft design was sketched (Figure 2.1) to decide on the initial parameters and see what assumptions are needed for the design.

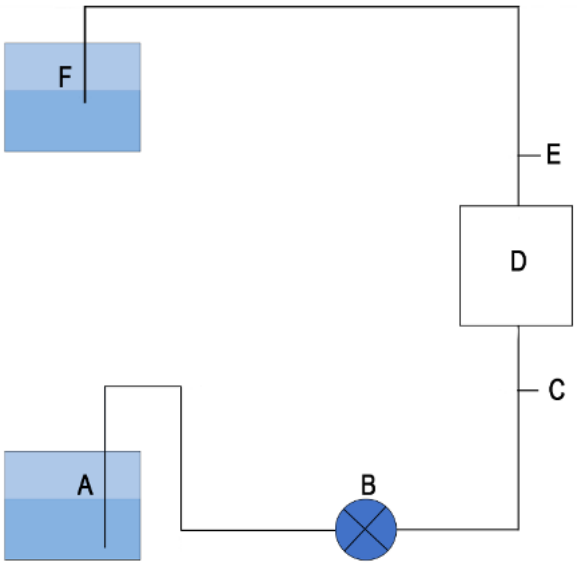

Figure 2-1. An initial sketch of the planned design. A: fluid level in the reservoir, B: peristaltic pump, C: lower pressure transducer, D: Magnetic Resonance Imaging (MRI) instrument, E: upper-pressure transducer, and F: fluid in the upper reservoir

2.1.2 Energy Balance Calculations

Assumptions were made to proceed with the engineering calculations. The assumptions are listed below:

- *Fully developed flow*
- *Newtonian fluid*
- *Steady state*

- *Incompressible fluid*
- *No slip-on pipe wall*
- *Laminar flow*

Considering the size of the MR system to be used and its location in the laboratory, 4 90^{o} elbows, and 2 T pipes were planned to be installed initially.

The mechanical energy equation used in the design calculations is shown in Equation 2.1 (Çengel & Cimbala, 2010).

$$\frac{P_2-P_1}{p}+\frac{1}{2\alpha}\left[(V_2^2)_{av}-(V_1^2)_{av}\right]+g(z_2-z_1)+W_s+\sum F=0 \qquad (2.1)$$

The pump purchased for the system is a peristaltic pump (SHENCHEN LABS3/UD15, China) and has the option to adjust the 'rpm' of the pump. To convert the 'rpm's to velocity values a calibration was established for the tube diameter of 8mm. The calibration plot is given in Figure 2.2. Distilled water was used as the model fluid for design calculations at 20^{o}C (ρ=998.23 kg/m^3) (Sahin et al., 2016).

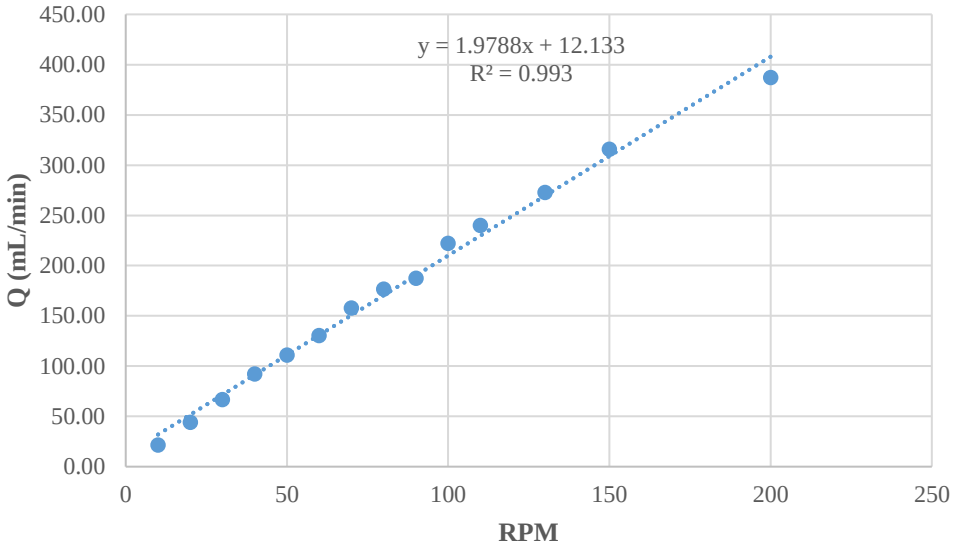

Figure 2-2. Pump calibration curve

2.1.3 Determining the Parameters for a Fully Developed Flow in a Pipe

A fully developed flow is needed to have correct rheological calculations. It is observed, when a straight pipe's length is traversed by a fluid with a fully developed velocity profile as a result of the viscous effects caused by the shear stress between the fluid's particles and pipe wall (White, 1991). Each fluid particle flows along a streamline with a constant axial velocity in fully developed laminar flow (Figure 2.3), and the velocity profile v(r) is unaffected by the flow direction. The velocity component in the direction normal to flow is 0 everywhere because there is no motion in the radial direction (Poole & Ridley, 2007).

Calculations were made at different flow rates for 3 different pipe diameters and the results are given in Table 2.1. Reynolds number was calculated as;

$$Re = \frac{Dv\rho}{\mu} \qquad (2.2)$$

Viscosity and density of water at 20 ^{o}C was used for *Re* number calculations.

Table 2.1. Reynolds number and velocity calculations for different flow rates and different pipe diameters

V (mm/s)	*Re (D=8 mm)*	*Re (D=6 mm)*	*Re (D=4 mm)*
1.00	7.94	6.00	3.97
5.00	39.72	29.66	19.86
10.00	82.00	60.20	39.98
30.00	240.00	180.05	119.68
60.00	479.25	360.10	239.63
160.00	1277.57	960.27	638.65
330.00	2641.20	1997.03	1317.00
500.00	3991.57	2997.00	1996.45

In the flow systems, the inlet region is the region where the fluid in the pipe cannot completely form the full flow profile (Figure 2.3). In this region, the velocity still changes in the axial direction (Çengel & Cimbala, 2010). This is not desired in an MR system since the MR image quality is affected adversely otherwise. For this reason, the length of the entrance area was calculated first. This information was also important to determine the positions where the MRI system and pressure sensors would be placed in the final model.

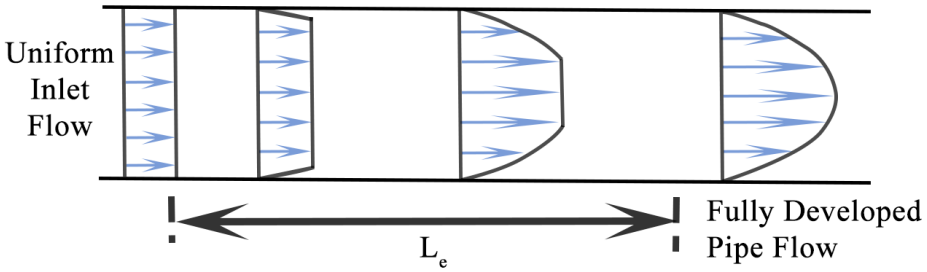

Figure 2-3. Hydrodynamic entrance length

In many MR flow imaging studies conducted by other researchers, it was stated that laminar flow was required (Arola, Barrall, Powell, McCarthy, et al., 1997; McCarthy et al., 1992; McCarthy & Kerr, 1998). For systems with laminar flow, the entrance region length is calculated with the following equation (Durst et al., 2005);

$$\frac{L_e}{D} = 0.06 * Re \qquad (2.3)$$

where L_e is the entrance length, D is pipe diameter, and Re is the Reynolds number. As seen in Equation 2.3, Reynolds number and pipe diameter are the two parameters that affect the inlet zone length. In Table 2.1., Re number less than 2100 indicates laminar flow, and from the table can be seen that in the flow velocity range which is restricted by MRI capability. With MRI, flow velocity less than 0.65 m/s was found to be measurable (Lew et al., 2007). The flow is in laminar region mostly. Hence, pipe diameter is relatively negligible in this flow behavior circumstance.

At this point, it was decided that any pipe diameter that keeps the system operating in the laminar region is suitable for the system. And since our goal is to design an MR Imaging flow system with high quality images, it has been deemed appropriate to choose the maximum pipe diameter that will increase the signal aspect ratio. Figure 2.4 shows the relationship between Reynolds number and inlet zone length for a pipe diameter of 8 mm.

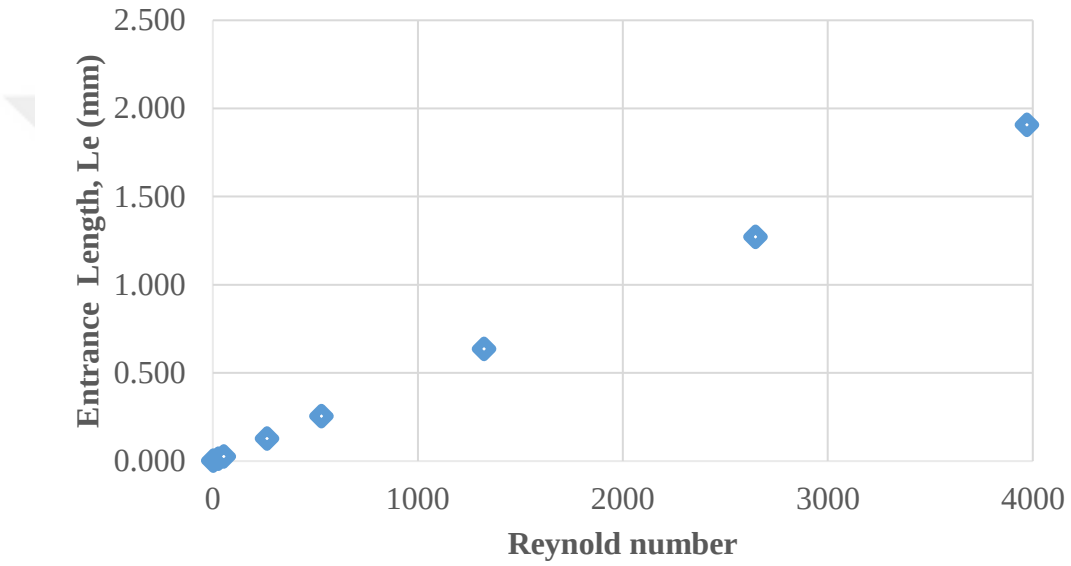

Figure 2-4. Relationship between Reynold number and inlet zone length for the selected pipe diameter (8mm)

As can be seen in Figure 2.4, to operate the system at different flow rates, to stay within the *laminar zone boundary* (*Re*=2100) for water where one of the toughest fluid due to low shear rate, the system needs at least 1-meter-long inlet zone. This value has also been considered in the future placement of the MRI system and pressure sensors.

2.1.4 Selection of the Proper Tubing and Diameter

One of the most important requirements of performing quantitative analysis in MRI is the requirement of high '*Signal to Noise Ratios*' (McCarthy & Kerr, 1998). Signal-to-noise ratios > 100 is usually looked for in quantitative image analysis. The higher this ratio, the more reproducible the data received from the signal. To increase this value, the sample measurement area should be used at the maximum dimensions in the radio frequency coil of the MRI system. The inner diameter of the rf coil in the MRI device that is used in this study is 10 mm. One of the limitations of the tubing selection is usually the inner diameter of the commercially available tubing. Since the designed system is preferred to be used for food applications, it was desired to have a tubing material that is acid resistant. Hence, 'Teflon' was selected as the proper material. The wall thickness (the difference between the pipe outer diameter and the inner diameter) of the Teflon pipes that are commercially available is mostly around 2 mm. For this reason, the pipes through which the flow will be provided can have a maximum internal diameter of 8 mm.

2.1.5 Design of a Pulsation/Pressure Dampener

In the design of the system a peristaltic pump was used. One of the problems associated with the use of a peristaltic pump in MR imaging is the 'pulsation' of the pump. This pulsation effect caused a blur in the images and prevented the development of laminar flow. A representative MR image with and without pulsation is given in Figure 2.5. As seen in the figure, flow is affected adversely due to the pulsation.

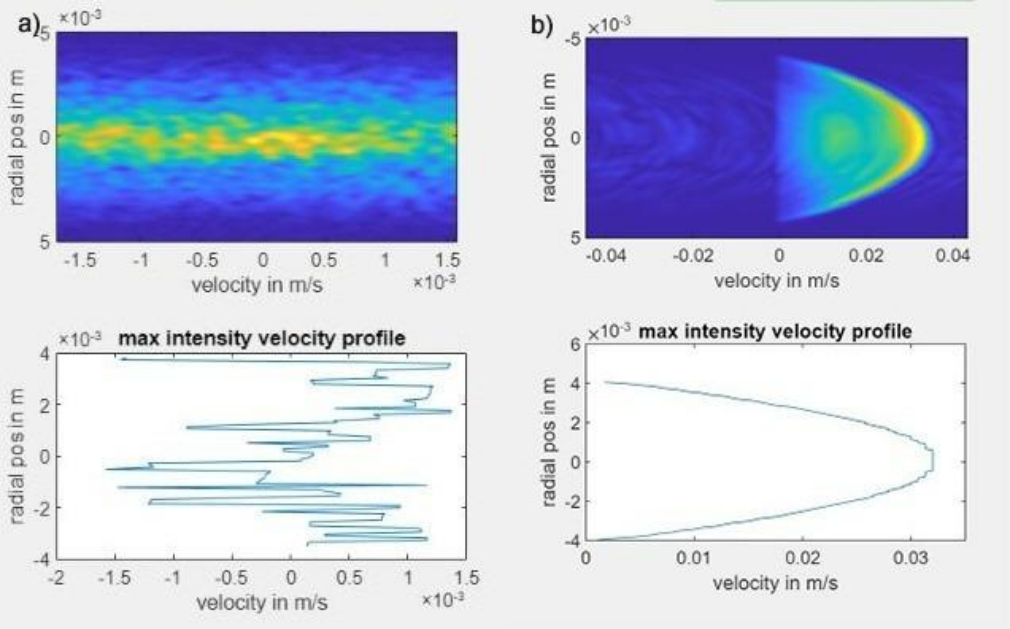

Figure 2-5. Flow MR images in the absence (a) /presence (b) of dampener

The pressure fluctuation created by the peristaltic pump in the pipe can also be seen in Figure 2.7 with the use of a flow dampener (McComb, 2014).

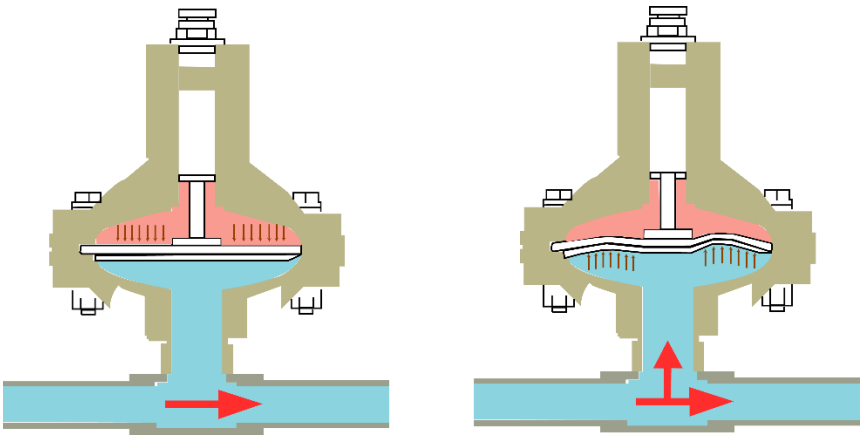

Figure 2.6. Pulsation dampener with pipe system in low pressure state and in high pressure state

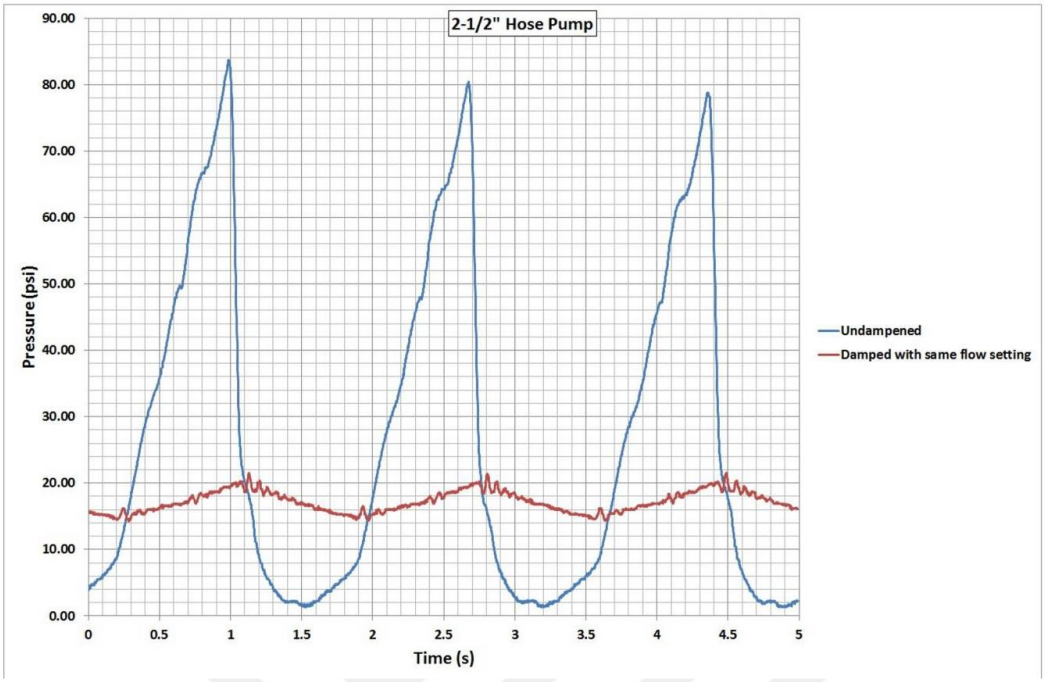

Figure 2-7. In-pipe hydrodynamic pressure change – (▬) without pressure dampener and (▬) with pressure dampener (McComb, 2014)

To overcome the pulsation effect, usually flow/pulsation dampeners are used. The purpose of the pulsation dampener is to stabilize the discharge flow and pressure and lessen the pulsation produced during operation.

The dampener can be thought of as a reservoir located just at the outlet of the pump, to absorb the sudden intra-pipe pressure created by the pump and to stabilize the flow rate by completing the gap in the flow when the pressure drops. One of the most important challenges of the dampener design is the correct adjustment of the volume of the reservoir and the pressure to keep the flow rate constant. If the pressure difference is higher than it should be, the space will be filled with more liquid, which will increase the flow rate. On the other hand, if the amount of liquid accumulated in the reservoir is low, sufficient damping will not be provided.

As can be seen from Figure 2.7, the peristaltic pump working with a flow dampener can provide mostly constant pressure and flow. Calculations to determine the volume of dampener required were made by considering the following assumptions and equations (McComb, 2014).

Assumptions:

- *Isentropic process*
- *80% air-filled flow damper*
- *Pump factor constant: 0.73 (from the pump specification manual)*

Volume formula of flow damper with known minimum and maximum pressure;

$$V_d = \frac{V_p * f_d * \left(\frac{P_2}{P_1}\right)^{\frac{1}{n}}}{V_{pr} * \left(\left(\frac{P_2}{P_1}\right)^{\frac{1}{n}} - 1\right)} \qquad (2.4)$$

Pressure formula with pump constant and volume of flow dampener;

$$P_2 = \left(\frac{V_d * V_{pr}}{V_d * V_{pr} - V_p * f_d}\right)^n * P_1 \qquad (2.5)$$

- *P_1: minimum pressure in the flow dampener (Pa)*
- *P_2: maximum pressure in the flow dampener (Pa)*
- *F_d: Pump factor fixed*
- *V_{pr}: air fill (%)*
- *V_d: flow dampener volume (ml)*
- *V_p, (dosage volume, ml)*
- *n: gas constant used*

Calculations started with the assumption of a flow rate of 500 ml/min. P_1 value is the hydrodynamic pressure of the liquid in the pipe in the system. This is the lowest pressure value that can be obtained while the pump is dosing. For the calculation of

the P_1 value, the points between the entry point to the flow dampener and the collection unit were selected, and P_1 pressure was calculated using the mechanical energy equations (2.1) in this interval. The mechanical energy balance is set between inside the dampener and the surface of collection tank. The pressure at the point where it reaches the collection unit is the atmospheric pressure (Figure 2.8). In addition, considering that, the volumetric flow rate does not change and taking the friction factor loss from its connections into count, the P_1 pressure is calculated as 113,600 Pa.

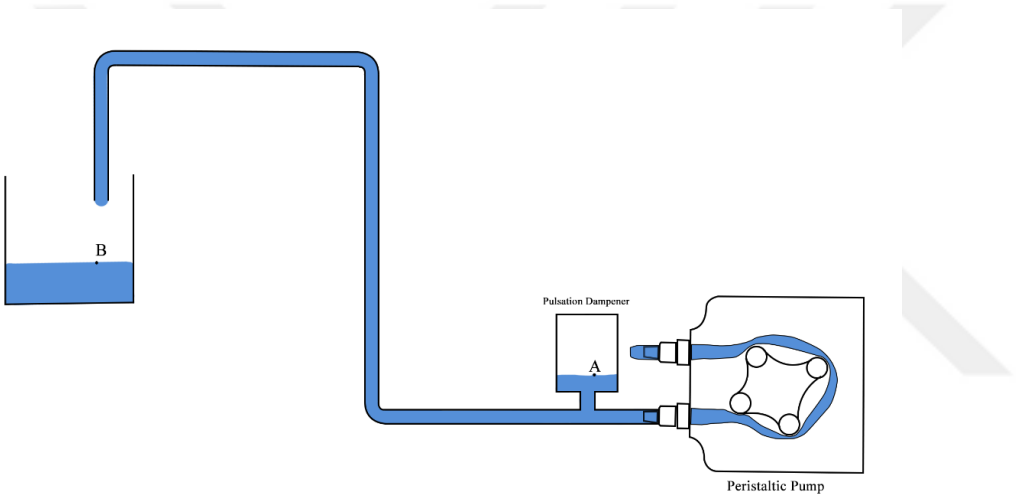

Figure 2-8. MRI flow system with pulsation dampener

After this step, the two unknowns in the flow damper equations V_d (dampener volume (ml) and P_2 were found as follows by 'the trial-and-error method (Table 2.3).

Table 2.2. Parameter values used in flow dampener calculation

Parameters	*Values*
Q (ml/min)	500
Pump factor constant, f_d	0.73
V_p, (pulse volume, ml)	3.382
V_{pr}, percent fill (%)	0.80, 0.85, 0.90
P_1 (Pa)	113600
P_2 (Pa)	120000
$(P_2/P_1)^{1/n}$	1.04

Table 2.3. Flow dampener volume calculations

	Dampener Volume (ml)		
	Flow rate	*Flow rate*	*Flow rate*
V_{pr} (% fill)	*100 ml/min*	*500 ml/min*	*800 ml/min*
80	80.4	80.4	80.4
85	75.6	75.6	75.6
90	71.4	71.4	71.4

Theoretically, the volume of the flow dampener was found to be approximately 80 ml when the system is assumed to be 80% air filled (V_{pr}).

2.2 3D Design of Flow MR System

According to calculations, the drawings to physically position the flow assisted MRI system were made using the KeyCreator software version 2015 (Kubotek Corporation, Japan), so that a realistic approach could be obtained. The design is given in Figure 2.9. Photo of the real system is also provided in Figure 2.10.

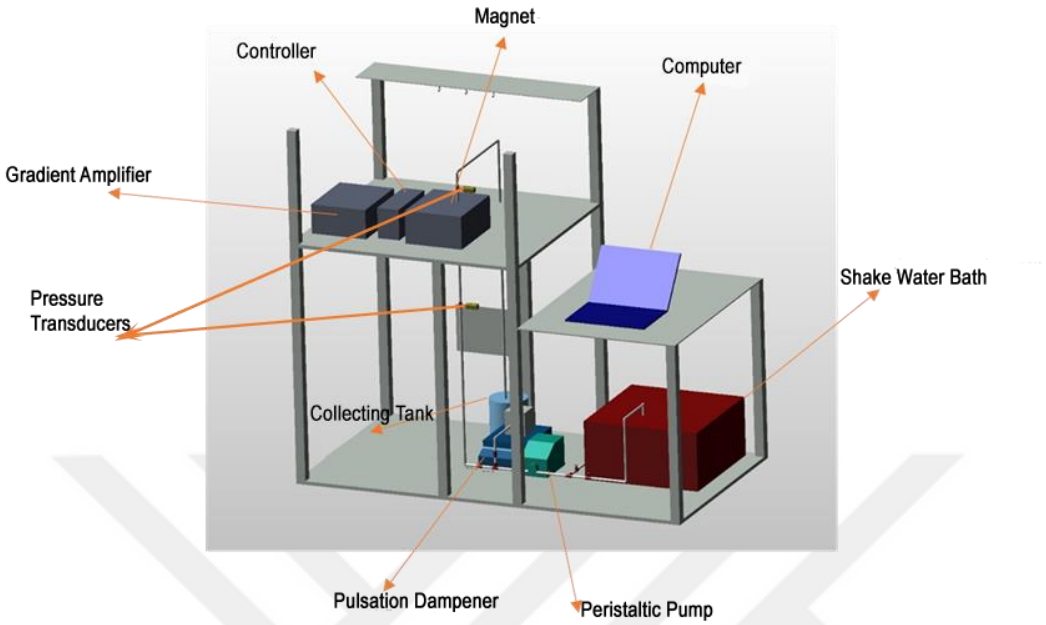

Figure 2-9. 3D model of the flow assisted MRI system

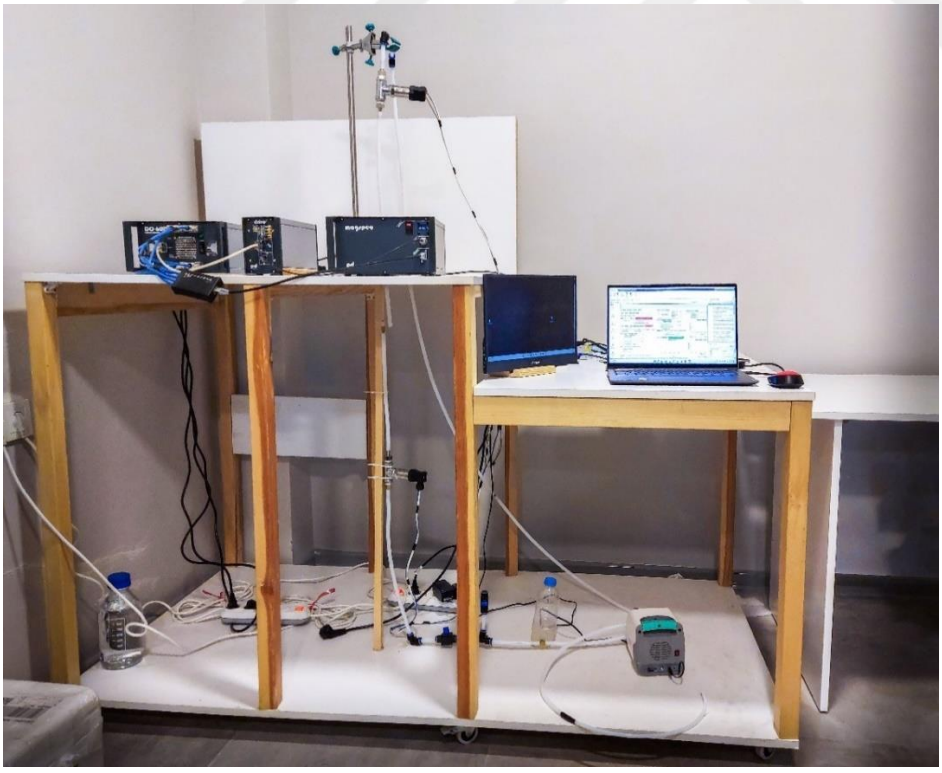

Figure 2-10. The lab scale assembled flow assisted MRI System

2.3 Preparation of Test Samples for the Flow MR System

All design calculations were done by using ‘distilled water’ as the fluid of interest. Later the system was tested for whole cow milk (MİS SÜT, Sakarya, Türkiye) as Newtonian fluids and almond milk (Alpro, Kırlareli, Türkiye) and methylcellulose (Sigma-Aldrich, U.S.A.) solutions at different concentrations as non-Newtonian fluids. Methylcellulose was selected because it is highly abundant and used as a thickener for many different food formulations. Methylcellulose was tested at four different concentrations 0.1, 0.5, 1.0, and 2.0 (w/w)%. Methylcellulose was dissolved in distilled water under vigorous stirring with magnetic stirrer overnight (Nasatto et al., 2015).

2.4 Determination of Time Domain NMR Parameters

In addition to flow imaging experiments, relaxation times (T_1, T_2) and self-diffusion coefficient measurements (D) were also made. The sequence and parameters are given in Table 2.4, 2.5, and 2.6. TD-NMR parameters were also associated with the flow parameters as discussed in the next section.

Table 2.4. T_1-Saturation recovery experiments parameters

Parameters	*Values*
Number of points	20
Number of averages	1
Delay time	2500-2800

Table 2.5. T_2-CPMG experiments parameters

Parameters	*Values*
Estimated T_2 (ms)	180-2400
T_2 Estimated min (ms)	10
T_2 Estimated max(ms)	200-2500
Number of averages	2
TR (ms)	1000-12500

Table 2.6. Pulse gradient spin echo experiments (PGSE) for self-diffusion coefficient measurements

Parameters	*Values*
Number of points	15
Echo time (ms)	20
Delay time	2800

2.5 Acquisition of MR Image

A benchtop MRI system (Pure Devices GmbH, Germany) operating at the ^1H frequency of 24.15 MHz, equipped with gradient amplifier (*Grad x: max 1.229 in T/m, Grad y: max 1.230 in T/m, and Grad z: max 1.515 in T/m*) and rf coil of 10 mm was used. Images were acquired using a *Pulsed Gradient Spin Echo sequence* with the following parameters. MATLAB (Mathworks Inc, Version 2022a, U.S.A.) based user interface VISCO_MR3 (McCarthy Engineering, Davis, U.S.A) was used for image acquisition. The following parameters needs to be entered to the software for image acquisition:

- *Predelay (ms):* Predelay is set based on the T_1. The longer the predelay the greater the T_1 recovery time.

- *Velocity encoding steps:* Affects the resolution of the image. The higher encoding steps, the longer the experiment time and the better the resolution is.
- *# Averages:* Directly affects the signal to noise ratio. The higher the average the longer acquisition time is and higher quality images are obtained.
- *Shear rate (s^{-1}):* Correct shear rate value that is observed in the flow should be entered to construct the correct velocity profile. But for unknown samples, it is hard to calculate and not applicable. Hence, shear rate is calculated from the flow rate which is correlated with rpm and corrected in the system by checking the quality of the image.

Table 2.7. Shear rate reference table according to rpm of the pump in the flow system

RPM	*Shear rate (1/s)*
10	7.11
20	14.66
30	22.15
40	30.67
50	36.92
60	43.34
70	52.46
80	58.63
90	62.29
100	73.83
110	79.74
130	90.61
150	104.92
200	128.61

2.5.1 Procedures to Follow in MR Imaging

Following the loading of sample to the system and setting up the parameters described above, MRI system is ready to run. The steps for conducting a full flow imaging experiment are described as follows:

- **Setup**: The tubing system should be filled with the fluid sample that is going to be tested. Pressure sensors (*pressure transducer*) should be checked thoroughly for presence of air bubbles on the sensor.
- **Measure offset**: The pressure transducer might have some shifted results. When the flow system is filled up, Transducer Offsets should be measured.
- **Calibration of the magnet**: Calibration should be made when the pipe is full of fluid, and the pump is turned off. Calibration time depends on the T_1 of the sample. Magnetic field homogeneity, frequency and rf pulse durations are determined.
- **Flow Parameters Input**: Capillary diameter, distance between pressure transducers, fluid density, and flow orientation (H – horizontal; V – vertical) are entered to the system.

2.5.2 Processing of MR Data

The image generation is made by following steps following the data acquisition:

1. Image data is zero-filled twice to increase the matrix size;
2. Gaussian filtering is applied to decrease the noise;
3. Fourier transformation is applied to the data set;
4. Image is constructed (Fig. 2.11)
5. Velocity profile is extracted from the image data by selecting the pixels with the maximum intensity in the velocity direction for each radial value (Figure 2.11.). Any amplitude value below 10% of the maximum image intensity is disregarded.

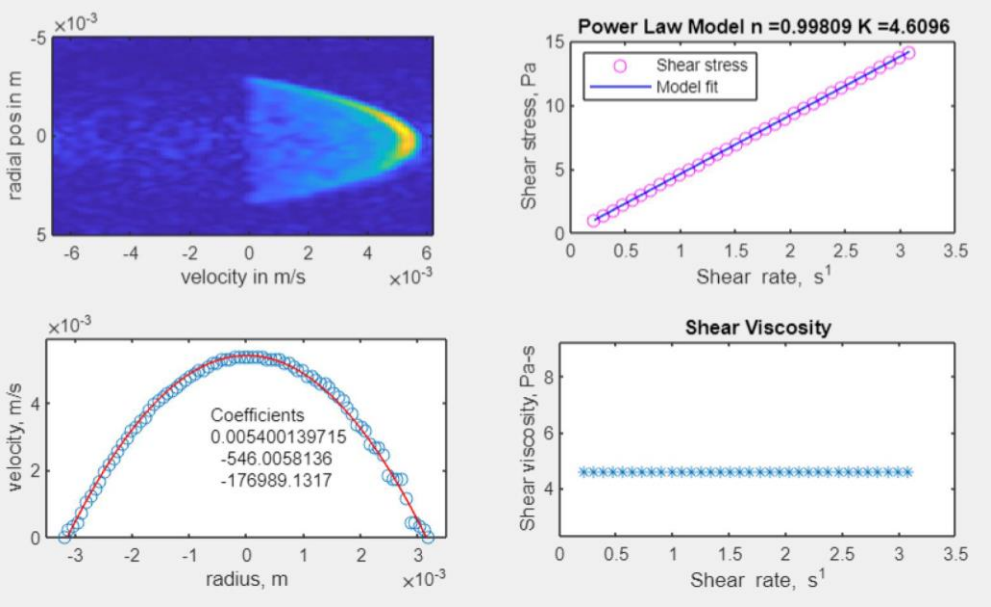

Figure 2-11. Output of the velocity image of water

2.5.3 Processing of Velocity Profile

To make quantitave analysis on the velocity profiles, procedures in similar studies were followed ((Arola, Barrall, Powell, Mccarthy, et al., 1997; Tozzi et al., 2014; Wichchukit et al., 2006; Yoon & McCarthy, 2002). The velocity profile obtained in previous steps was fit to a 4th even-order polynomial.

$$v(r) = ar^4 + br^3 + cr^2 + dr + e \qquad (2.6)$$

where $v(r)$ is velocity as a function of r; a, b, c, d, e are constants and r is radius. 1st derivative of the polynomial is taken along the r variable and shear rate is obtained.

$$\frac{dv}{dr} = \dot{\gamma} = 4ar^3 + 3br^2 + 2cr + d \qquad (2.7)$$

where $\dot{\gamma}$ is shear rate. Shear stress data are calculated for each radial position from the pressure drop.

$$\tau = \frac{(\Delta P)R}{2L} \qquad (2.8)$$

Shear viscosity that is calculated by dividing shear stress by shear rate is also plotted in the rheogram (Figure 2.11). Then, the rheogram is fit to an appropriate model such as the power law model. A MATLAB code was used to analyze the data. The code is provided in Appendix B.2.

2.6 Determination of Rheological Properties by Using the Conventional System

The rheological behavior of all solutions was also determined using a bob (25mm stainless steel) and cup rheometer (stainless steel) (KINEXUS, Malvern Instruments, UK). Samples are measured at 20^{o}C. Shear stress and shear rate values are used to determine the rheological behavior of the fluid.

2.7 Determination of Density

Density of the samples are measured using a pycnometer (Brand Blaubrand, Germany).

CHAPTER 3

RESULTS AND DISCUSSION

In this section, quality of an MR image was discussed, results obtained with the designed system were examined and compared to the conventional rheometer results. The rheology results were also compared with the Time Domain NMR parameters (T_1, T_2 relaxation times and *Self-diffusion Coefficient*). In addition, challenges of the MRI assisted flow system were discussed.

3.1 Data Quality

A good quality image cannot be obtained just by entering the theoretical parameters to the software. Trials should be performed to get the perfect velocity profile. It is likely that a high SNR image could not yield good rheology data or vice versa.

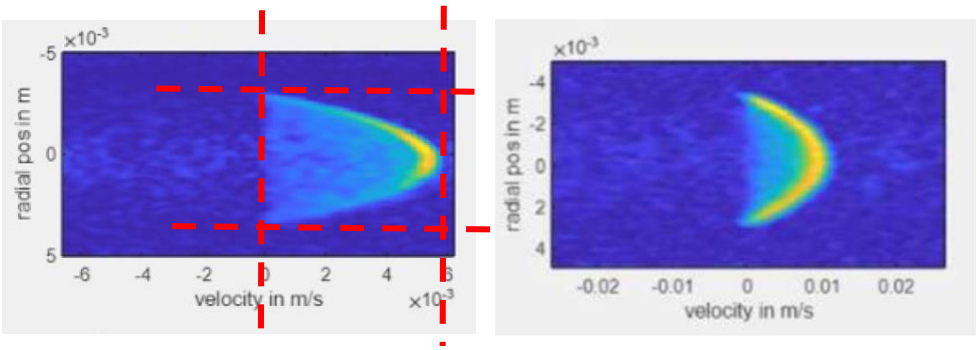

Figure 3-1. Example flow images yielding different 'quality' rheology data

For instance, the images in Figure 3.1 are good enough for velocity data even though the right one has less signal-to-noise ratio. To have a good transition from the image to the velocity profile; *seeing the edges of the flow signal (red dashed region in*

Figure 3.1) is a necessity. Imaging artifacts that occur due to incorrect parameter settings can also lead to improper velocity profiles. Examples are given in Figure 3.2.

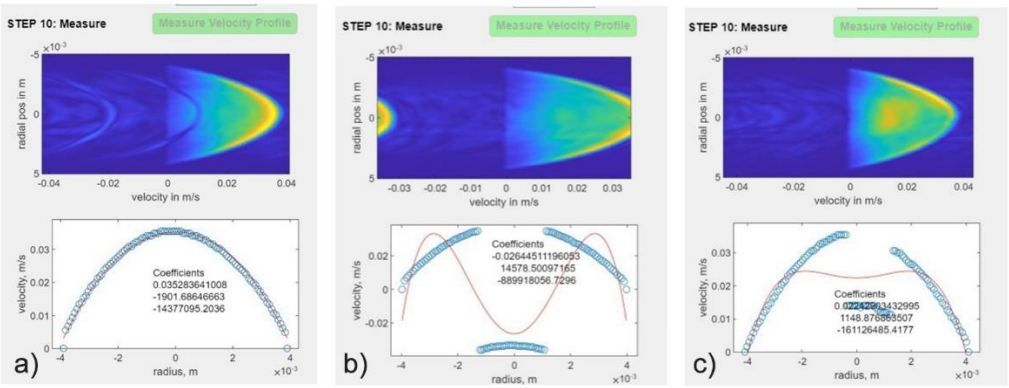

Figure 3-2. Example flow images yielding different 'quality' rheology data and their corresponding velocity profiles; a) proper image, b) image with aliasing (wraparound) artifact c) another artifact

The proper flow image is the one shown in Figure 3.2a. The artifact in Figure 3.2b is the image processing artifact that is also called aliasing. Aliasing is caused by miscalculation of data outside of FOV (*Field of View*) after the maximum phase encoding gradient. Then, for the part outside of FOV, it is assumed as the lowest frequency field and added to the beginning part of the image. That occurs when the estimated shear rate is too low and can be solved if it is increased. The artifact in Figure 3.2c is likely to have been caused be by a high shear rate value. Hence, it should be decreased.

3.2 Testing the MR System for Flow Measurements

The design of the MR system was performed as described in Chapter 2. To test whether the system is working properly or not; whole milk as a Newtonian fluid,

almond milk, and methylcellulose solutions at different concentrations were used as non-Newtonian fluids.

One of the most important challenges of the MR flow systems is the deviations observed with the conventional rheometer measurements. Viscosity values, consistency index, and flow behavior indexes show differences between MR and conventional rheometers. To understand these deviations preliminary trials were performed and compared with the expected results. In that scope, initially the test of the system was done with almond and whole milk samples. Rheological characterization of the samples was performed using a conventional rheometer first and later the samples were run through the MR system at different condition and comparison with the theoretical calculations were done and the deviations of the design systems were reported.

3.2.1 Conventional Rheometer Measurements of Milk Samples

Shear stress/shear rates (*for 10 samples*) and shear viscosity/shear rate (*a representative sample*) plots of the milk samples are provided in Figure 3.3 and Figure 3.4 respectively. As can be seen in Figure 3.4, as expected, whole milk showed Newtonian behavior whereas almond milk exhibited a shear thinning behavior. K and n values for the 'power law' fitting confirmed that whole milk is *Newtonian* (n~1) whereas almond is *non-Newtonian* (n<1) (Table 3.1). 'K' value of whole milk which is equivalent to the *Newtonian viscosity* was consistent with the previous studies (Alhamdan, 2002).

As seen in Figure 3.4, almond milk differentiated itself from regular milk samples as exhibiting a typical *shear thinning behavior*. Consistency index (K) was *10* times larger than whole milk and *n* value was found as 0.783 (Table 3.1). In the product label, it is stated that almond milk includes locust bean gum and gellan gum as stabilizers. Fat content is also reported as ~1.1%. Despite the lower fat content values

than whole milk, higher consistency values were observed. This was explained by *viscosity enhancing* effects of the used hydrocolloids. In Figure 3.4, it is seen that there are absurd jumps in data between shear rate 60 – 65 (1/s). This trend of jump in every measurement for different samples as well, and when we check the fitting R^2, it is approximately 0.99. Thus, that is assumed instrumental error and since it does not change the fitting, it is neglected.

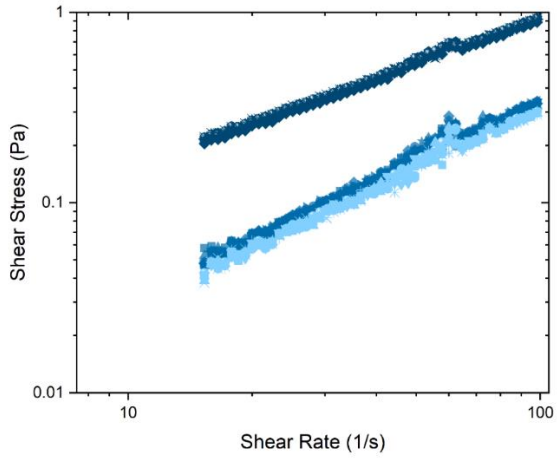

Figure 3-3. Shear stress vs. shear rate data of skim 10 milk (●), whole milk (●), and almond milk (●) samples

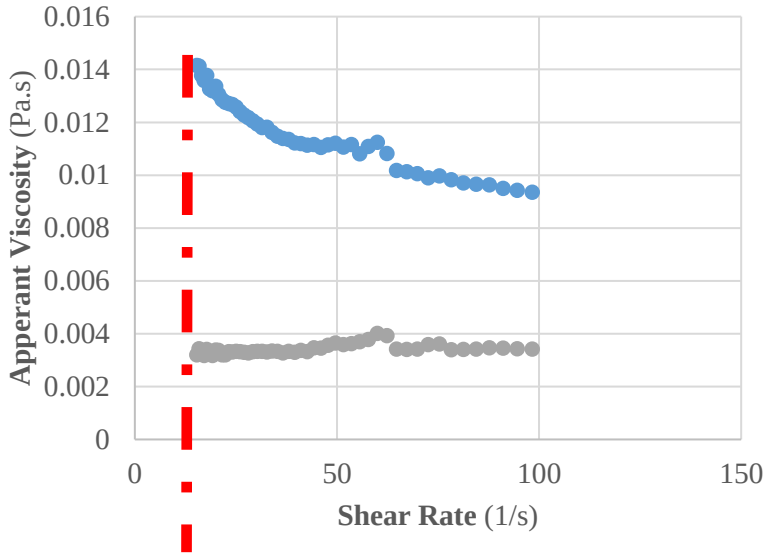

Figure 3-4. Representative shear viscosity vs. shear rate plots for whole milk, and almond milk

Table 3.1. Power law fitting values of milk samples*

Sample Name	*K (Pa.s^n)*	*n*
WM	0.0032±0.0001[a]	1.019±0.006[a]
ALM	0.0254±0.0005[b]	0.783±0.004[b]

**Lower case letters denote significant difference at 95% confidence level.*

Hussain et al (2017) showed that 1% locust bean gum (LBG) solution had ~0.3 Pa.s apparent viscosity at 10 s^{-1} shear rate indicating that gum concentration in almond milk was much less than 1% (Hussain et al., 2017). The other common hydrocolloid that is used in almost all plant-based milk is the gellan gum. Gellan gum is an extracellular polysaccharide secreted by the microorganism *Sphingomonas elodea* (ATCC 31461) previously referred to as *Pseudomonas elodea* (Sworn & Stouby, 2021). Commercially it is manufactured by a fermentation process. *Gellan* gum's properties make it ideal to be used as a thickener, suspension agent and stabilizer in many food and beverage products. Gellan gum can keep the beverage's ingredients

stable and suspended and prevents sediment formation at the bottom of the beverage. In a previous study where effect of temperature, shear rate and NaCl was investigated on gellan gum, it was shown that at the shear rate of 10 s^{-1}, it had an apparent viscosity of 200 cP at the concentration of 1 g/L. In almond milk case, the apparent viscosity was found to be 14 cP. Thus, gellan gum concentration was used less than 1% like LBG.

3.2.2 Preliminary Trials for the Operability of the MRI System

Since the system was set up from the basics, to determine the operating conditions of the flow tests, trials were conducted at different 'rpms' of the pump. Almond milk and whole milk were used as the test fluids. As detected in the conventional rheometer experiments, whole milk showed *Newtonian* whereas almond milk showed *non-Newtonian behavior*.

To test whether the MR flow system is working properly, at first, flow trials were tested at different 'rpm' values of the pump. Flow images of whole milk and almond milk, obtained at different 'rpm' values and the corresponding velocity profiles are given in Figure 3.5, 3.6 and Figure 3.7, 3.8 respectively. The 'rpm' trials (*20, 30, 40, 50, 60*) were just tested once to confirm the 'operability' of the physical system. That is why there is <u>one</u> measurement at each flow rate. As discussed later, at a selected *rpm* for all milk samples, measurements were also conducted in three replicates.

As described in the previous sections; a velocity image is constructed by a *Pulse Gradient Spin Echo Sequence* and it is important to enter the 'correct' shear rate value for the proper image. For the correct shear rate value, the reference table in Section 2 (Table 2.7) was used as a starting point and depending on the image quality and the velocity profile, it was adjusted. The imaging protocol was designed such

that the gradient strength in the sequence was adjusted based on the shear rate. If the maximum shear rate in the pipe is higher than the entered value 'ladder shaped' profiles are obtained, and this causes misinterpretation in the MRI data. The crucial point is to obtain a smooth parabolic curve for the velocity profile.

One of the first points that needs to mentioned is the presence of artifacts in the velocity images (Figure 3.5, 3.7, 3.9). Since the signal to noise ratio in the flow edges were sufficiently high, artifacts did not cause the problems that were described before and thus images were used to acquire the velocity profiles.

In order to check whether the system was operating correctly; the average velocity values obtained from the flow images were used to calculate the theoretical pressure difference for whole and almond milk. For whole milk (*as being Newtonian*) the following equation was used;

$$\Delta P = \frac{8\mu L \vartheta_{av}^2}{R^2} + \rho g z \qquad (3.1)$$ (Şahin et al., 2016)

For almond milk the pressure drop equation for power law fluids were used (Goloshevsky et al., 2005) (Equation 3.2)

$$\Delta P = \left(\frac{2KL}{R}\right) * \left(\vartheta_{av} * \frac{z+3}{R}\right)^{\frac{1}{z}} + \rho g z \; ; z = \frac{1}{n} \qquad (3.2)$$

Parameters used in Equation 3.1 and 3.2 are listed in Table 3.2. For the viscosity and power law constants, conventional rheometer results obtained in the previous section were used. Density values were obtained experimentally as described in Section 2.7.

Table 3.2. Parameters used for the theoretical calculation of the pressure drop (ΔP)

Parameter	*Value*	*Unit*
$\mu_{\text{whole milk}}$	0.0032	Pa.s
Consistency index for almond milk (K)	0.0254	Pa.s
Flow behavior index for almond milk (n)	0.783	-
$\vartheta_{\text{av-whole milk}}$	0.0099-0.0306	m/s
$\vartheta_{\text{av-almond milk}}$	0.0095-0.0281	m/s
R	4.00E-03	mm
$\rho_{\text{whole milk}}$	1082.4	kg/m^3
$\rho_{\text{almond milk}}$	1064.0	kg/m^3
g	9.80655	m/s^2
L	0.77	m

Table 3.3. Comparison of the theoretical and experimental pressure measurements for almond & whole milk

rpm	*Whole Milk*				
	ΔP Theory (Pa) (1)	*ΔP Experimental (Pa) (2)*	*% error*	*1/2*	*RMSE*
20	7827.53	5352	31.63	1.46	**1.2**
30	7834.18	5128	34.54	1.53	
40	7839.978	4984	36.43	1.57	
50	7844.41	4945	36.96	1.59	
60	7853.03	4681	40.39	1.68	
rpm	*Almond Milk*				
	ΔP Theory (Pa) (1)	*ΔP Experimental (Pa) (2)*	*% error*	*1/2*	*RMSE*
20	7875.4	6020	23.56	1.31	**3.8**
30	7903.46	5616	28.94	1.41	
40	7924.18	5178	34.66	1.53	
50	7939.84	4722	40.53	1.68	
60	7955.74	4344	45.4	1.83	

As seen in the Table 3.3, % error in pressure measurements were in the range of 23-45%. The error rate was quite high, and it was explained by the inherent error due to ‘pressure transducers’ and the manually built dampener. However, it was quite interesting to note that the correlation between theoretical and experimental pressure values were significantly correlated ($p<0.05$, $r>0.99$). The two independent data set with high correlation indicated that ‘a transducer/dampener’ correction factor could decrease the discrepancy between the data sets. Relation between experimental and theoretical pressure values were also expressed by a linear relationship as seen in Figure 3.10. Linear expressions had a regression coefficient ~0.98 with slopes of -0.0391 and -0.0464 for whole and almond milk respectively. In addition, root mean square error values are given in Table 3, where it is used to measure the differences between predicted values and theoretical values. The less the RMSE is, the more accurate the approximation is. For both whole milk and almond milk, RMSE’s are 1.2, and 3.8 so it is counted as reliable model since those are small numbers compared to actual values(Ali et al., 2023). Figure 3.5 shows residual distribution for the plots in Figure 3.10. The residuals are distributed around zero axis homogeneously.

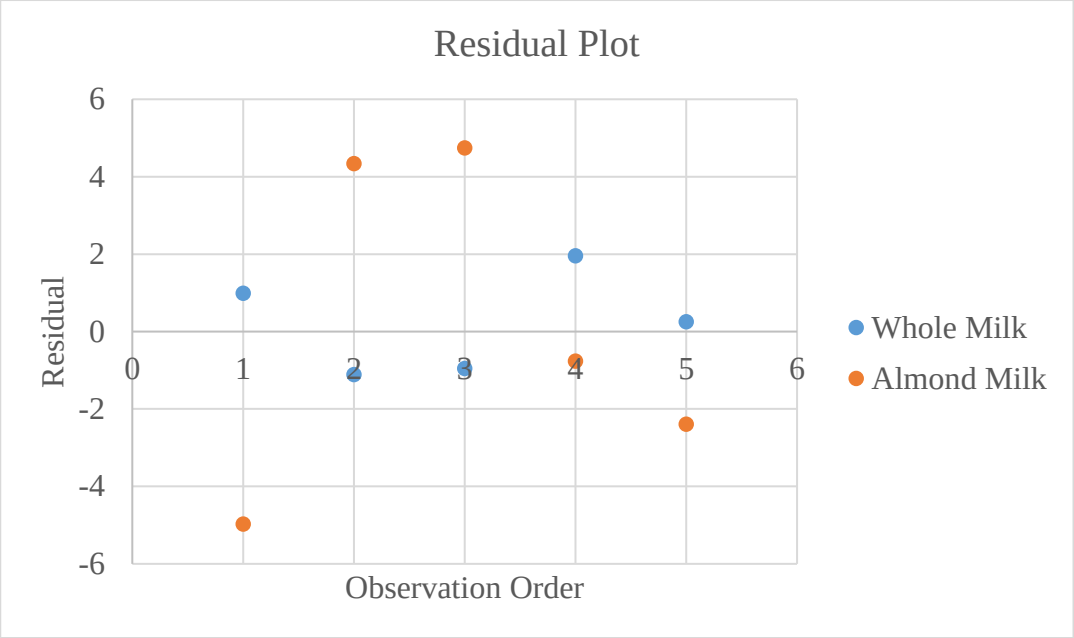

Figure 3-5 Residual plot of fitting

As illustrated by the conventional rheometer experiments, almond milk had higher viscosity values them whole milk. It was interesting to note that when the 'pump' rpm values were lower than 50; *error rates of the pressure difference* in almond milk were lower in magnitude compared to whole milk. To explore this better, velocity values at the wall were extracted from the images to see whether slip was more prominent in the low viscosity milk sample. As seen in Table 3.4, velocity values were not available for the almond milk at the wall indicating low signal and almost zero velocity, whereas velocity values at the pipe wall were observable for whole milk samples indicating that slipping could have contributed to the high error rates at lower rpm values.

Table 3.4. Comparison of wall slip velocity at different rpm for almond and whole milk

	Wall Velocity (m/s)	
rpm	*Whole Milk*	*Almond Milk*
20	0.0018	-
30	0.0027	-
40	0.0044	-
50	0.0038	0.0021
60	0.0041	0.0029

The reason for higher error rates in almond milk above 50 rpm was explained with the higher pressures created in the dampener with increased ‘rpm’ values and possible ‘air bubbles’ in the transducer.

The experiment results in this section confirmed that the system is working as planned, but there is an **inherent error** on the system due to the dampener and the pressure transducer and the reported value of pressure difference should be corrected to find the ‘correct’ rheological parameters. To find a correction factor, it was hypothesized that more samples should be tested and a relationship between the corrected and theoretical values should be calculated.

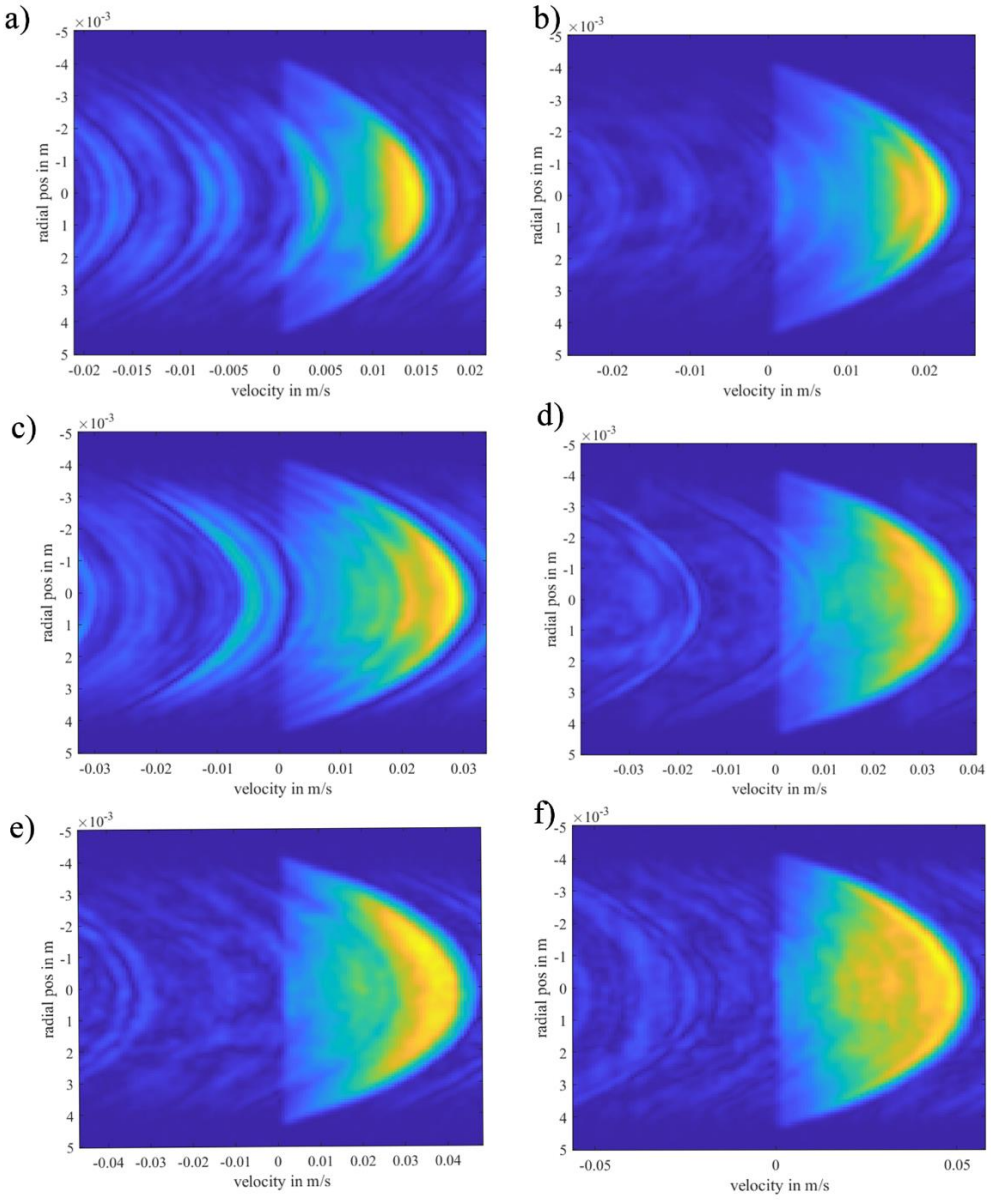

Figure 3-6. Velocity images of whole milk vs. radial position at different rpms of the pump a) 20 rpm b) 30 rpm c) 40 rpm d) 50 rpm e) 60 rpm, and f) 70 rpm

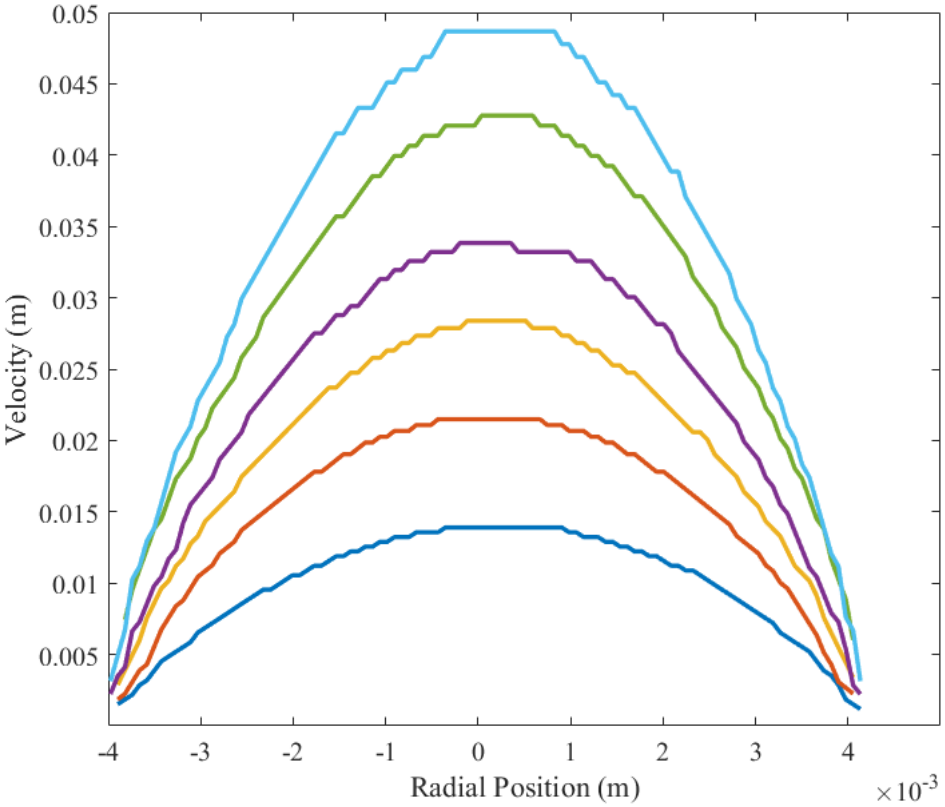

Figure 3-7. Velocity distribution for whole milk: 20 rpm (0.0099 m/s), 30 rpm (0.0153 m/s), 40 rpm (0.0200 m/s), 50 rpm (0.0236 m/s), 60 rpm (0.0306 m/s), and 70 rpm (0.0339 m/s)

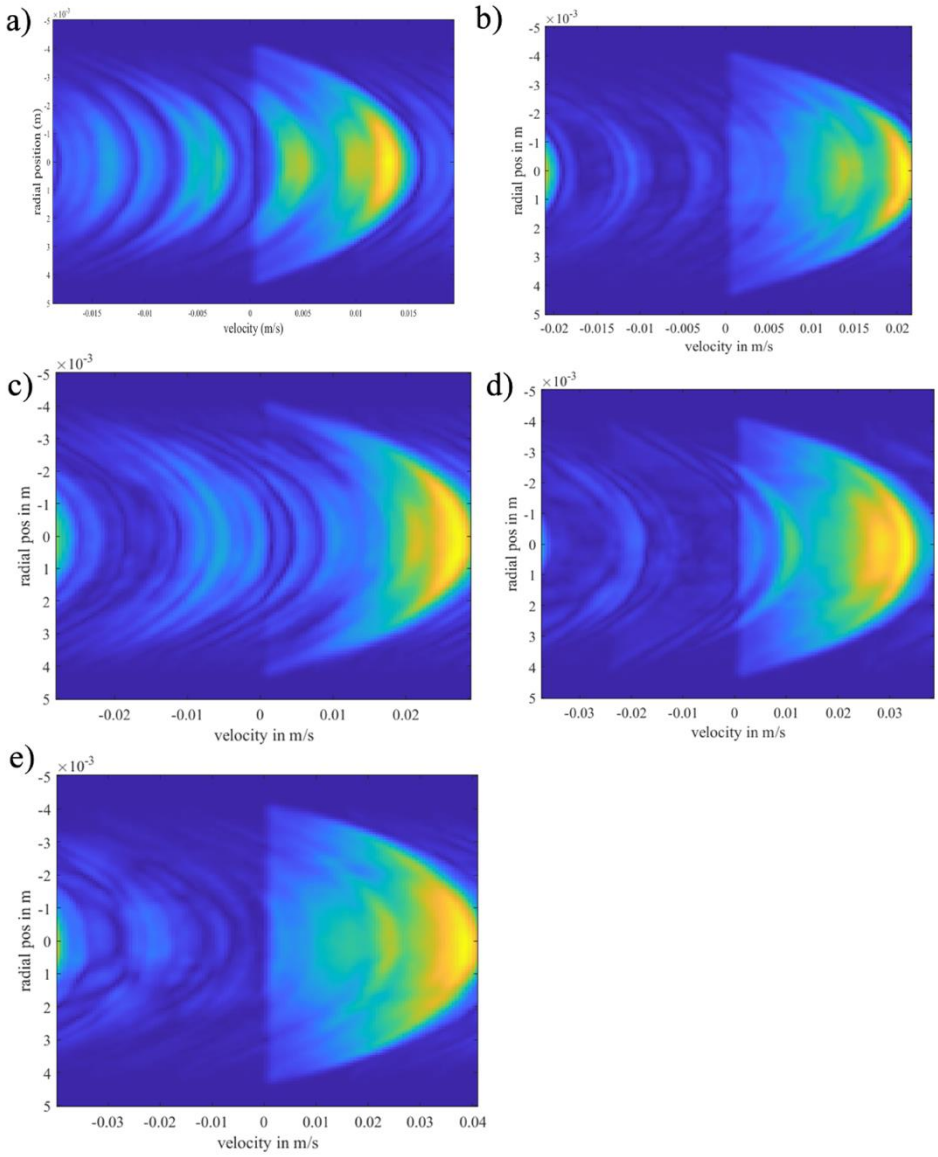

Figure 3-8. Velocity images of almond milk vs. radial position at different ‘rpms’ of the pump a) 20 rpm, b) 30rpm c) 40rpm, d) 50rpm, and e) 60rpm

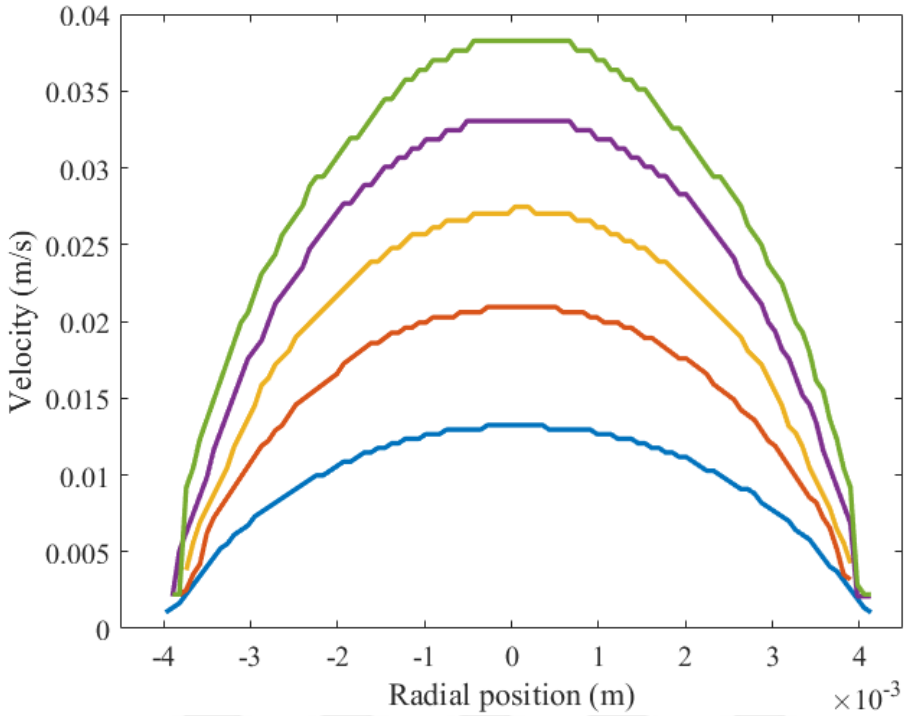

Figure 3-9. Velocity profile of almond milk obtained at different rpm values of the pump: 20 rpm (0.0095 m/s), 30 rpm (0.0155 m/s), 40 rpm (0.0203 m/s), 50 rpm (0.0241 m/s), and 60 rpm (0.0281 m/s)

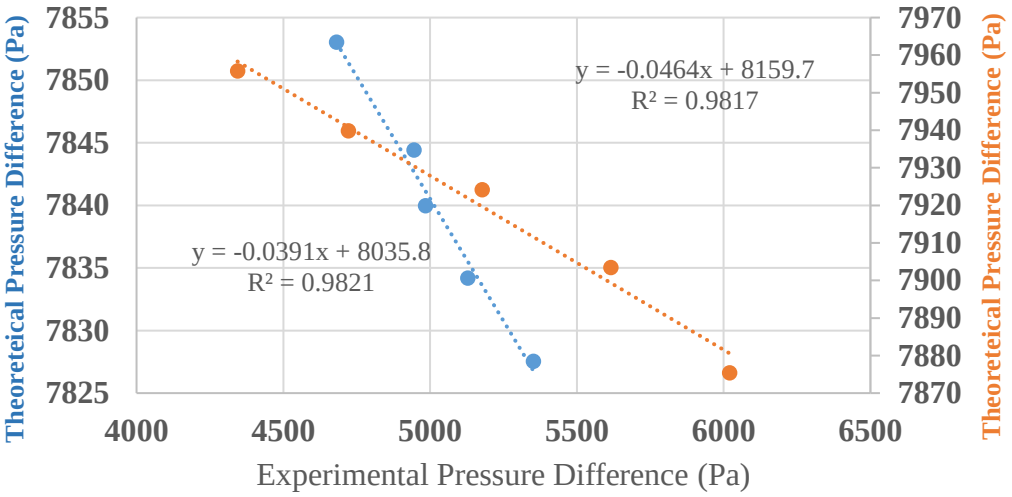

Figure 3-10. Relation between theoretical vs experimental pressure values; ▬ whole milk; ▬ almond milk

3.2.3 Examining the Flow System with Another Sample Set: *Methyl Cellulose Solutions*

The **inherent error** in the pressure measurements was confirmed in the previous section. In this part of the study, methyl cellulose solutions were prepared in replicates and flow measurements were performed. This time, experiments were performed at a fixed rpm. Preliminary trials showed that good quality images for MC solutions were acquired at 40 rpm. Thus at 0.1, 0.5, 1 and 2% concentrations of the MC, experiments were performed. In order to calculate the deviations in pressure measurements as performed for milk samples; rheological constants of MC solutions were required. Thus, as in the case of milk samples rheological characterization of the MC samples were first done by using a conventional rheometer.

3.2.3.1 Rheological Parameters of Methyl Cellulose Solutions Using a Conventional Rheometer

Shear stress/shear rates plots for the MC solutions at four different concentration are given in Figure 3.10. Shear viscosities are given in Figure 3.11 and power law fittings are also provided in Table 3.5. Shear thinning behavior was much less at concentrations of 0.1 and 0.5%. Behavior was consistent with the studies of previous researchers (Morozova et al., 2018).

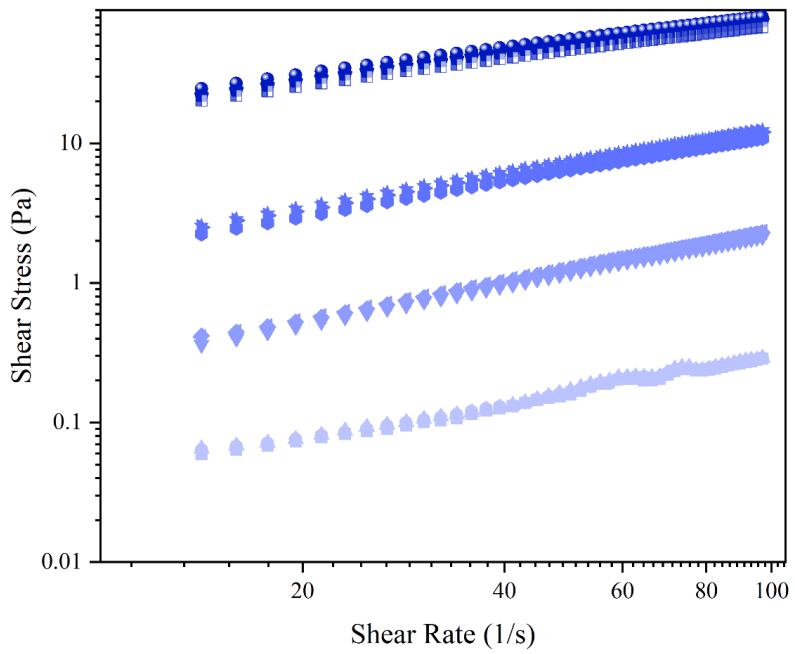

Figure 3-11. Shear stress (Pa) vs shear rate (1/s) of methyl cellulose; 0.1% MC (w/w), 0.5% MC, 1% MC, and 2% MC

Table 3.5. Power law fitting values of 'MC' solutions

MC Concentration (%)	*K (Pa.s^n)*	*n*	R^2
0.1	0.0059±0.0005^d	0.85±0.02^b	0.99
0.5	0.0349±0.0162^c	0.91±0.04^a	0.99
1.0	0.3031±0.0281^b	0.80±0.01^c	0.99
2.0	4.8338±0.5900^a	0.60±0.02^d	0.99

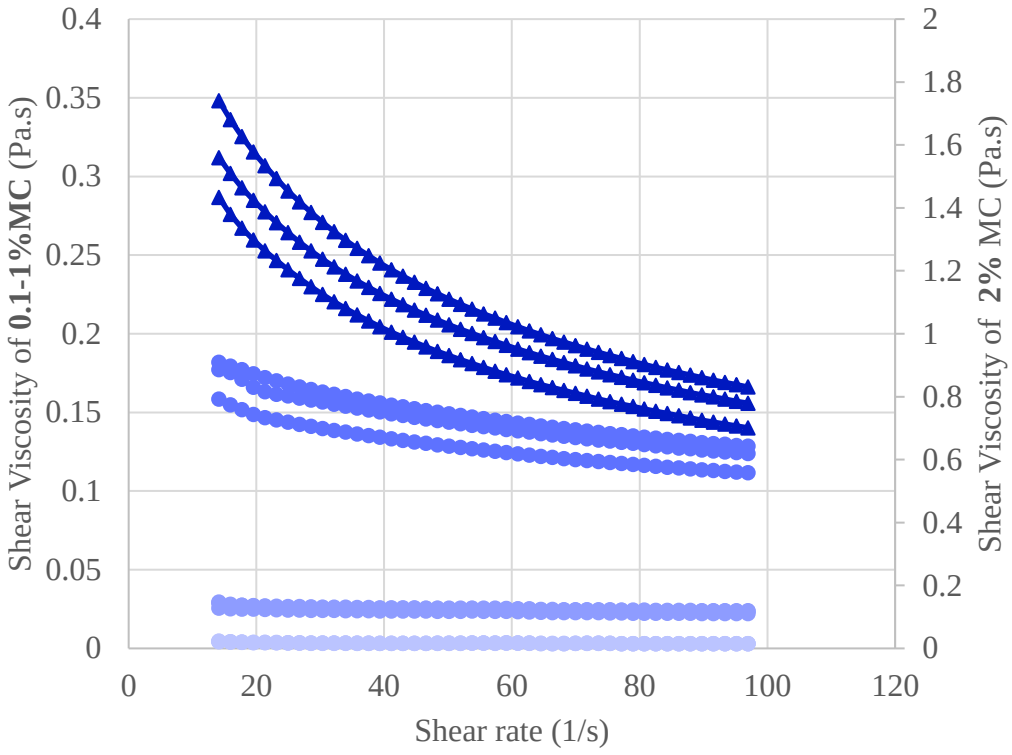

Figure 3-12. Shear viscosity (Pa.s) vs Shear rate (1/s); ● 0.1% (w/w) MC, ● 0.5% MC, ● 1% MC, and ▲ 2% MC

3.2.3.2 MR Flow Tests for the MC Solutions

Average velocities of the MC solutions were also calculated as in the milk samples (Figure 3.12).

This time for each concentration three replicates were run. Theoretical pressure differences were calculated using Eqn. 3.2 and the K and n values obtained from the conventional rheometer. Results are given in Table 3.6. MC MR flow experiments were performed at the pump rpm of 40. As seen in the table, % error differences changed in the range of 25-30% except 2% MC solution which was significantly almost 15-20 more viscous than the other solutions. During these measurements the dampener used for previous measurements leaked out and reconstructed. But still the results deviated more compared to other concentrations.

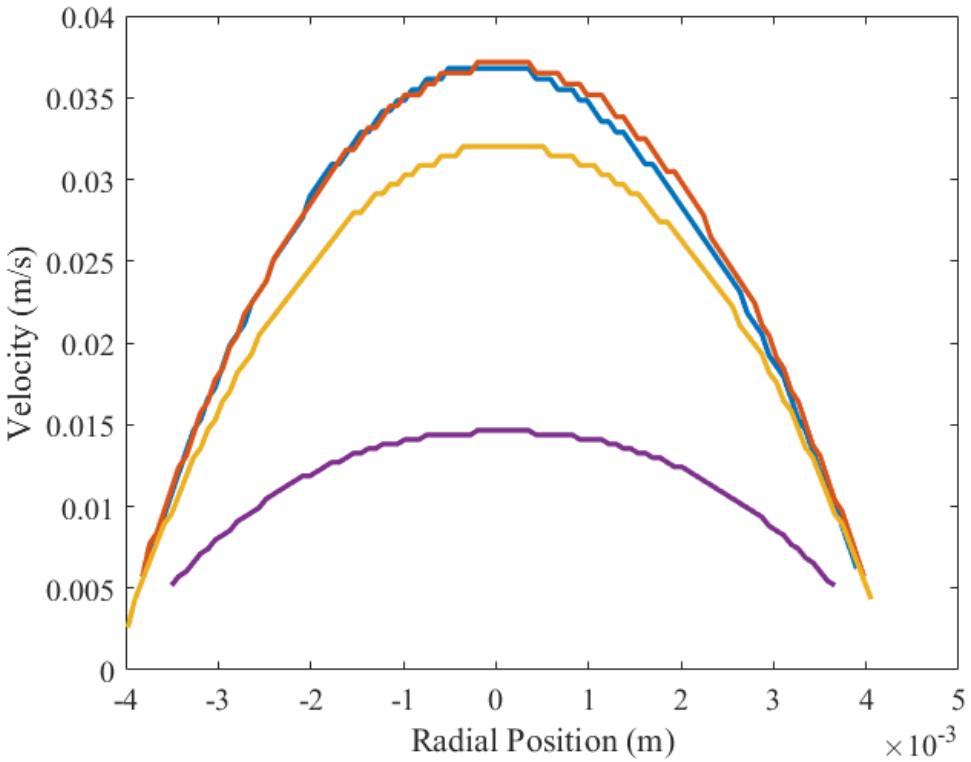

Figure 3-13. ● 0.1% (w/w) MC (Vavg = 0.0266 m/s), ● 0.5% MC (Vavg = 0.0266 m/s), ● 1% MC (Vavg = 0.0227 m/s), and ● 2% MC

Table 3.6. Comparison of the theoretical and experimental pressure measurements for methylcellulose solutions at different concentrations

Sample	V_{avg} *(m/s)*	*ΔP_Theory (Pa)*	*ΔP_Real (Pa)*	*% Error*	*ΔP_Theory/ΔP_Real*
MC-0.1	0.0266	9559.26	6663	30.29	1.43
MC-0.1	0.0261	9560.61	6700	29.92	1.43
MC-0.1	0.0276	9563.88	6773	29.18	1.41
MC-0.5	0.0193	9752.81	7200	26.18	1.35
MC-0.5	0.0266	9861.84	7300	25.98	1.35
MC-0.5	0.0228	9822.06	7271	25.97	1.35
MC-1.0	0.0227	11438.34	8100	29.19	1.41
MC-1.0	0.0221	11206.63	8188	26.94	1.37
MC-1.0	0.0224	11454.37	8288	27.64	1.38
MC-2.0	0.0117	20592.23	9897	51.94	2.08
MC-2.0	0.0066	18277.46	9300	49.12	1.97
MC-2.0	0.0135	20552.55	9600	53.29	2.14

A linear relation was also observed for between the theoretical and calculated values and results are plotted in Figure 3.14. As seen in the plot, 2% solution deviated significantly from other concentrations (*red circle*). Since theoretical and real data are compared, RMSE value gives comparable value regarding to the degree of the model fit. In Figure 3.14, RMSE value of the fit is found to be 211.9, which looks big compared to the ones for the milk samples but when we think of the magnitude of the ΔP that is obviously bigger than the ΔP of the milk samples. On the other hand, 211.9 is small compared to ΔP so it can be counted as reliable model.

3.2.4 Evaluation and Interpretation of the MR Flow Data

Results until now showed that;

Imaging system works perfectly and yield good quality velocity images. But the pressure transducer/dampener causes an inherent deviation in the pressure difference values, which in turn would affect deviations from calculation of the rheological constants. Thus, what could have been done?

As the first step, K and n values were calculated from the velocity profiles using the approach in Section 2. R^2 values for the flow MR fittings were also above 0.99.

K values obtained from flow MR system were obviously higher than the conventional ones. When ANOVA was conducted on the n values for conventional and flow MRI methods for the 'n' values, no significant difference was detected ($p>0.05$) (Appendix, Table A.6). For almond milk samples n values were also same whereas for whole milk samples n values were lower n flow MRI ($p<0.05$).

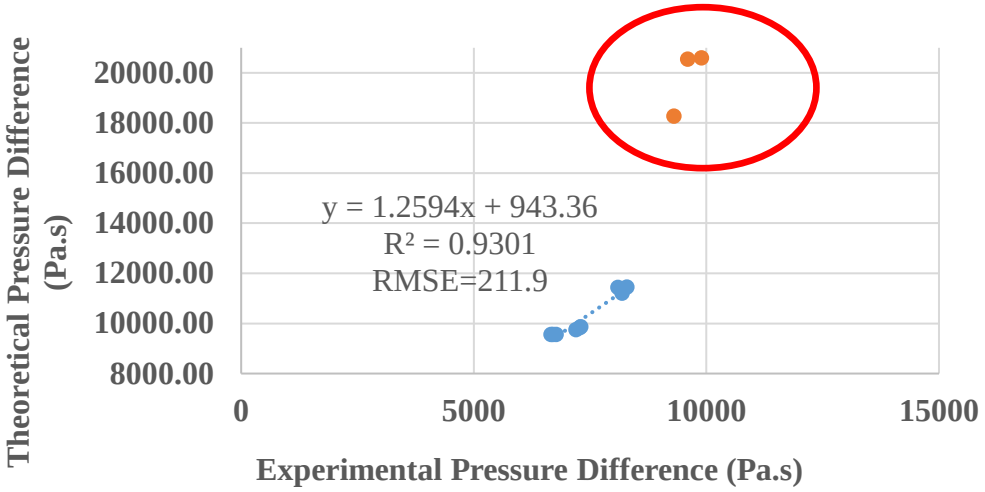

Figure 3-14. Relation between theoretical vs experimental pressure values for methylcellulose at different concentrations

Table 3.7. Parameter comparison of conventional and MR rheometers

	Conventional Rheometer (CR)		*Flow MRI*	
Sample	*K (Pa.s)*	*n*	*K (Pa.s)*	*n*
MC-0.1	0.0059 ± 0.0005^{d}	0.85 ± 0.02^{b}	0.258 ± 0.007^{a}	0.92 ± 0.01^{a}
MC-0.5	0.0349 ± 0.0162^{c}	0.91 ± 0.04^{a}	0.456 ± 0.081^{b}	0.84 ± 0.01^{b}
MC-1.0	0.3031 ± 0.0281^{b}	0.80 ± 0.01^{c}	0.671 ± 0.026^{c}	0.90 ± 0.02^{a}
MC-2.0	4.8338 ± 0.5900^{a}	0.60 ± 0.02^{d}	2.495 ± 0.460^{d}	0.63 ± 0.01^{c}
Whole Milk	0.0032 ± 0.0001^{B}	1.019 ± 0.006^{A}	0.035 ± 0.006^{B}	0.93 ± 0.02^{A}
Almond Milk	0.0254 ± 0.0005^{A}	0.783 ± 0.004^{B}	0.784 ± 0.008^{A}	0.76 ± 0.02^{B}

**Milk and MC samples, CR and Flow MRI data were examined separately for ANOVA. K and n values were also analyzed separately. Lower, upper-case letters denote significance difference at 95% confidence level (at different rows). Comparison of 'n' values for CR and Flow MRI for MC samples is provided in Table A.6.*

Only whole milk samples having a different ‘n’ value was explained by the non-zero wall velocities. The difference in K values was due to the different ‘*inherent error*’ on the pressure measurements as explained before.

Pearson correlation analysis was carried for all samples (MC + milk) between ‘K’ values obtained conventionally and from flow MRI system. Results showed a significant positive correlation with a correlation coefficient of 0.97 ($p<0.05$). However, a linear relationship was not obtained.

Hence, the current flow MR system was good at predicting flow behavior of fluids. However, deviations occurred especially for Newtonian fluids due to the violation of the ‘no slip’ condition.

The manually built-in dampener and the pressure transducer error rate were quite high but had a positive correlation between the theoretical pressure difference values. A correction factor could not be calculated for the overall system since; the susceptibility of the transducer and the dampener to different fluids were different.

However, the current design could be used to make a rheological comparison for different liquid systems.

3.2.5 Comparison of Rheological Data with the Time Domain NMR Parameters

Investigation of the rheological parameters with the TD-NMR Relaxation times is frequently explored (Alacik Develioglu et al., 2020; Dekkers et al., 2016; Kirtil & Oztop, 2016a). Relaxation times and self-diffusion coefficient of the samples were

all measured, and results are given in Table 3.8. As seen in the Table 3.7, methyl cellulose concentration had a significant effect on the relaxation times. Both T_1 and T_2 times decreased with increasing methyl cellulose concentration (Kirtil & Oztop, 2016a). Higher solute concentration and polymer entanglement thus trapping of water within the polymer chains resulted in shorter relaxation times.

The decrease in relaxation times was much more prominent for T_2 values whereas for T_1 even at 2% concentration T_1s were ~2.5s. For dilute systems, it is known that T_1 is strongly correlated with the water content (Kirtil & Oztop, 2015) and results confirmed this observation. Increase in solute concertation resulting in shorter relaxation times is not only observed in polymers but even for simple molecules like sugars the same trend was observed (Tas et al., 2022).

However, for milk samples the opposite behavior was observed. Almond oil a shear thinning and more viscous fluid compared to whole milk had significantly longer relaxation times ($p<0.05$). It seems that rather than the effect of the hydrocolloids, we see the effect of the fat content which was ~1.1% compared to 3% in whole milk. The other reason could be the milk proteins being better at decreasing the mobility of the water and emulsifying the fat in the system.

Relation between the consistency index and viscosity values were also explored (Table 3.9). For methyl cellulose samples, a positive and significant correlation was detected between the T_1, D and 'k' values whereas for milk samples this was not the case. A similar case was observed in the study of Kirtil et al (2016) where the emulsions produced by xanthan gum despite higher viscosity had longer relaxation times. So, in this study, it was also confirmed that the dependency of viscosity to relaxation times could be violated in emulsion systems.

Table 3.8. Time Domain NMR parameters for the MC solutions and milk samples

Sample	*T_1 (ms)*	*T_2 (ms)*	*Diffusivity (m/s^2) x 10^9*
MC-0.1	2890.5 ± 18.4^{a}	2402.3 ± 17.2^{a}	2.499 ± 0.014^{a}
MC-0.5	2795.6 ± 6.9^{b}	2093.8 ± 18.9^{b}	2.437 ± 0.020^{b}
MC-1.0	2722.9 ± 40.3^{b}	1727.0 ± 32.8^{c}	2.424 ± 0.011^{b}
MC-2.0	2510.1 ± 55.1^{c}	1183.3 ± 19.9^{d}	2.319 ± 0.019^{c}
Whole Milk	1547.4 ± 2.4^{B}	184.0 ± 3.2^{B}	1.920 ± 0.061^{B}
Almond Milk	1623.2 ± 14.4^{A}	551.7 ± 1.3^{A}	2.302 ± 0.007^{A}

**Milk and MC samples were examined separately for ANOVA. Lower, upper case letters denote significance difference at 95% confidence level (at different rows).*

Table 3.9. Pairwise Pearson Correlations for MC samples

Sample 1	Sample 2	*Correlation*	*95% CI for ρ*	*p-Value*
T_2	T_1	0.759	(-0.747, 0.995)	0.241
Diffusivity	T_1	0.992	(0.677, 1.000)	0.008*
k-MRI	**T_1**	**-0.962**	**(-0.999, -0.012)**	**0.038***
Diffusivity	T_2	0.798	(-0.700, 0.996)	0.202
k-MRI	T_2	-0.875	(-0.997, 0.542)	0.125
k-MRI	**Diffusivity**	**-0.953**	**(-0.999, 0.093)**	**0.047***

CHAPTER 4

CONCLUSION AND RECOMMENDATIONS

In this thesis, a bench top MRI system working at a field strength of 0.5 Tesla was converted to an *MR Flow device (MR Viscometer/Rheometer)* to make *online* rheological measurements. The physical setup was designed by performing engineering calculations. In most flow MR systems, either syringe pumps or transfer pumps are used. However, since this system would later be used for investigating the rheological changes in digestion fluids, a peristatic pump was selected. However, the 'pulsation' nature of the peristatic pump introduces distortion in the velocity image and thus affects the velocity profile. For that reason, a manual pulsation dampener was designed. When the flow experiments were tested, it was observed that the difference between theoretical and experimental pressure calculations were significantly high for high viscous fluids. That indicated that the designed dampener was not ideal for the high viscosity fluids. To overcome that problem the best solution would be to use a real dampener that can tolerate high pressures.

In the study, to test whether the design of the systems is matching with the theoretical calculations; *theoretical and calculated pressure* differences were calculated. Almond milk and whole milk were run at different flow rates and as the pressure in the dampener increased, the error rate of the calculated pressure difference increased. Afterwards, methyl cellulose solutions at different concentrations were also tested. Nevertheless, for different fluids, the relation between theoretical and calculated pressure differences were linearly related until the fluid becomes significantly viscous (*methyl cellulose at 2% concentration*).

Velocity profiles obtained from the images were used to calculate the flow characteristics of the fluids. Flow behavior indices, '*n*' of the fluids was not different ($p>0.05$) for the two measurement methods however there were order of magnitude difference in the *K* values but with a positive and significant correlation ($p<0.05$).

Throughout the study, a bench top MRI system was converted to a flow MR system that is operating with a peristatic pump successfully for differentiation rheological parameters. The main challenge that was faced was the *manually built-in pulsation dampener*. Once it is replaced with a real one; the pressure difference error is expected to decrease and the discrepancies in the 'K' values would diminish.

For future study, a fluid having a yield stress and a multiphase system liken an emulsion will be tested in the system and rheological characterization will be performed.

REFERENCES

Alacik Develioglu, I., Ozel, B., Sahin, S., & Oztop, M. H. (2020). NMR Relaxometry and magnetic resonance imaging as tools to determine the emulsifying characteristics of quince seed powder in emulsions and hydrogels. *International Journal of Biological Macromolecules*, *164*, 2051–2061. https://doi.org/10.1016/j.ijbiomac.2020.08.087

Alhamdan, A. M. (2002). Rheological properties of a newly nutritious dairy drink from milk and date extract concentrate (DIBBS). *International Journal of Food Properties*, *5*(1), 113–126. https://doi.org/10.1081/JFP-120015595

Ali, F., Sarwar, A., Ilahi Bakhsh, F., Ahmad, S., Ali Shah, A., & Ahmed, H. (2023). Parameter extraction of photovoltaic models using atomic orbital search algorithm on a decent basis for novel accurate RMSE calculation. *Energy Conversion and Management*, *277*, 116613. https://doi.org/10.1016/J.ENCONMAN.2022.116613

Arola, D. F., Barrall, G. A., Powell, R. L., Mccarthy, K. L., & Mccarthy, M. J. (1997). Use of nuclear magnetic resonance imaging as a viscometer for process monitoring. In *Chemical Engineermg Science* (Vol. 52, Issue 13).

Arola, D. F., Barrall, G. A., Powell, R. L., McCarthy, K. L., & McCarthy, M. J. (1997). Use of nuclear magnetic resonance imaging as a viscometer for process monitoring. *Chemical Engineering Science*, *52*(13), 2049–2057. https://doi.org/10.1016/S0009-2509(97)00033-X

Bernstein, M., King, K., & Zhou, X. (2004). *Handbook of MRI Pulse Sequences*. Elsevier.

Bracewell R. (1986). *The Fourier transform and its applications*.

Callaghan, P. T. (1999). Rheo-NMR: nuclear magnetic resonance and the rheology of complex fluids. *Reports on Progress in Physics*, *62*(4), 599–670. https://doi.org/10.1088/0034-4885/62/4/003

Callaghan, P. T. (2006). Rheo-NMR and velocity imaging. In *Current Opinion in Colloid and Interface Science* (Vol. 11, Issue 1, pp. 13–18). https://doi.org/10.1016/j.cocis.2005.10.003

Callaghan, P. T. (2012). Rheo-NMR: A new window on the rheology of complex fluids. *EMagRes*, *1*(1), 155–168. https://doi.org/10.1002/9780470034590.emrstm0470

Callaghan, P. T., Eccles, C. D., & Xia, Y. (1988). NMR microscopy of dynamic displacements: k-space and q-space imaging. *Journal of Physics E: Scientific Instruments*, *21*(8), 820–822. https://doi.org/10.1088/0022-3735/21/8/017

Çengel, Y. A., & Cimbala, J. M. (2010). *McGRAW-HILL SERIES IN MECHANICAL ENGINEERING Anderson: Computational Fluid Dynamics: The Basics with Applications*.

Choi, Y. J., McCarthy, K. L., & McCarthy, M. J. (2005). A MATLAB graphical user interface program for tomographic viscometer data processing. *Computers and Electronics in Agriculture*, *47*(1), 59–67. https://doi.org/10.1016/j.compag.2004.08.001

de Freitas Maciel, G., de Oliveira Ferreira, F., & Fiorot, G. H. (2013). Control of instabilities in non-Newtonian free surface fluid flows. *Journal of the Brazilian Society of Mechanical Sciences and Engineering*, *35*(3), 217–229. https://doi.org/10.1007/s40430-013-0025-y

Dekkers, B. L., de Kort, D. W., Grabowska, K. J., Tian, B., van As, H., & van der Goot, A. J. (2016). A combined rheology and time domain NMR approach for determining water distributions in protein blends. *Food Hydrocolloids*, *60*, 525–532. https://doi.org/10.1016/j.foodhyd.2016.04.020

Durst, F., Ray, S., Ünsal, B., & Bayoumi, O. A. (2005). The Development Lengths of Laminar Pipe and Channel Flows. *Journal of Fluids Engineering*, *127*(6), 1154–1160. https://doi.org/10.1115/1.2063088

Giitz, J., Miillerb, D., Buggisch, H., & Tasche-Lara, C. (1994). NMR flow imaging of pastes in steady-state flows. In *Chemical Engineering and Processing* (Vol. 33).

Gladden, L. F., & Sederman, A. J. (2017). *Magnetic Resonance Imaging and Velocity Mapping in Chemical Engineering Applications*. https://doi.org/10.1146/annurev-chembioeng

Goloshevsky, A. G., Walton, J. H., Shutov, M. v., de Ropp, J. S., Collins, S. D., & McCarthy, M. J. (2005). Nuclear magnetic resonance imaging for viscosity measurements of non-Newtonian fluids using a miniaturized RF coil. *Measurement Science and Technology*, *16*(2), 513–518. https://doi.org/10.1088/0957-0233/16/2/025

Götz, J., & Zick, K. (2008). Rheo-NMR: Applications to Food. In *Modern Magnetic Resonance*.

Griffiths, H. J. (1997). MRI: The Basics. *Radiology*, *204*(1), 152–152. https://doi.org/10.1148/radiology.204.1.152

Harmonay, V. (2018). *MRI Gradient Coils :101*.

Hashemi, R. H., Bradley, W. G., & Lisanti, C. J. (2010). *MRI: The Basics* [BOOK]. Lippincott Williams & Wilkins.

Hussain, R., Singh, A., Vatankhah, H., & Ramaswamy, H. S. (2017). Effects of locust bean gum on the structural and rheological properties of resistant corn starch. *Journal of Food Science and Technology*, *54*(3), 650–658. https://doi.org/10.1007/s13197-017-2497-8

IMAIOS. (2019). *e-MRI Course*.

Kirtil, E., & Oztop, M. H. (2015). H Nuclear Magnetic Resonance Relaxometry and Magnetic Resonance Imaging and Applications in Food Science and Processing. *Food Enginnering*. https://doi.org/10.1007/s12393-015-9118-y

Kirtil, E., & Oztop, M. H. (2016a). Characterization of emulsion stabilization properties of quince seed extract as a new source of hydrocolloid. *Food Research International*, *85*, 84–94. https://doi.org/10.1016/j.foodres.2016.04.019

Kirtil, E., & Oztop, M. H. (2016b). 1H Nuclear Magnetic Resonance Relaxometry and Magnetic Resonance Imaging and Applications in Food Science and Processing. In *Food Engineering Reviews* (Vol. 8, Issue 1, pp. 1–22). Springer New York LLC. https://doi.org/10.1007/s12393-015-9118-y

Lavenson, D. M., Tozzi, E. J., Mccarthy, M. J., & Powell, R. L. (2011). Yield stress of pretreated corn stover suspensions using magnetic resonance imaging. *Biotechnology and Bioengineering*, *108*(10), 2312–2319. https://doi.org/10.1002/bit.23197

Lee, Y., Bobroff, S., & Mccarthy, K. L. (2002). Rheological characterization of tomato concentrates and the effect on uniformity of processing. *Chemical Engineering Communications*, *189*(3), 339–351. https://doi.org/10.1080/00986440212085

Lew, C. D., Alley, M. T., Bammer, R., Spielman, D. M., & Chan, F. P. (2007). *Peak Velocity and Flow Quantification Validation for Sensitivity-Encoded Phase-Contrast MR Imaging*.

Manneville, S., Bécu, L., & Colin, A. (2004). High-frequency ultrasonic speckle velocimetry in sheared complex fluids. *The European Physical Journal Applied Physics*, *28*(3), 361–373. https://doi.org/10.1051/epjap:2004165

McCarthy, K. L., Kauten, R. J., McCarthy, M. J., & Steffe, J. F. (1992). Flow profiles in a tube rheometer using magnetic resonance imaging. *Journal of*

Food Engineering, *16*(1–2), 109–125. https://doi.org/10.1016/0260-8774(92)90023-Y

McCarthy, K. L., & Kerr, W. L. (1998). Rheological Characterization of a Model Suspension during Pipe Flow Using MRI. *Journal of Food Engineering*, *37*(1–4), 11–23. https://doi.org/10.1016/s0260-8774(98)00079-x

McComb, D. (2014). *Sizing Pulsation Dampeners Is Critical to Effectiveness*.

Moratal, D., Valles-Luch, A., Marti-Bonmati, L., & Brummer, M. (2008). k-Space tutorial: an MRI educational tool for a better understanding of k-space. *Biomedical Imaging and Intervention Journal*, *4*(1). https://doi.org/10.2349/biij.4.1.e15

Morozova, S., Schmidt, P. W., Metaxas, A., Bates, F. S., Lodge, T. P., & Dutcher, C. S. (2018). Extensional Flow Behavior of Methylcellulose Solutions Containing Fibrils. *ACS Macro Letters*, *7*(3), 347–352. https://doi.org/10.1021/acsmacrolett.8b00042

Nakatani, A. I., Poliks, M. D., & Samulski, E. T. (1990). NMR Investigation of Chain Deformation in Sheared Polymer Fluids. In *Macromolecules* (Vol. 23). https://pubs.acs.org/sharingguidelines

Nasatto, P. L., Pignon, F., Silveira, J. L. M., Duarte, M. E. R., Noseda, M. D., & Rinaudo, M. (2015). Methylcellulose, a Cellulose Derivative with Original Physical Properties and Extended Applications. *Polymers 2015, Vol. 7, Pages 777-803*, *7*(5), 777–803. https://doi.org/10.3390/POLYM7050777

Poole, R. J., & Ridley, B. S. (2007). Development-length requirements for fully developed laminar pipe flow of inelastic non-Newtonian liquids. *Journal of Fluids Engineering, Transactions of the ASME*, *129*(10), 1281–1287. https://doi.org/10.1115/1.2776969

Pope, J. M., & Yao, S. (1993). *Concepts in Magnetic Resonance* (Vol. 5).

Sahin, S., Sumnu, G., Isci, A., Sakıyan, O., & Hamamci, H. (2016). *Fluid Flow, Heat & Mass Transfer in Food Systems* (1st ed., Vol. 1). NOBEL AKADEMİK YAYINCILIK EĞİTİM DANIŞMANLIK TİC. LTD. STİ.

Şahin, S., Şumnu, S. G., Hamamcı, H., İşçi, A., & Şakıya, Ö. (2016). *Fluid Flow, Heat & Mass Transfer in Food Systems* (1st ed.). NOBEL AKADEMİK YAYINCILIK EĞİTİM DANIŞMANLIK.

Shapley, N. C., Brown, R. A., & Armstrong, R. C. (2004). Evaluation of particle migration models based on laser Doppler velocimetry measurements in concentrated suspensions. *Journal of Rheology*, *48*(2), 255–279. https://doi.org/10.1122/1.1647560

Sworn, G., & Stouby, L. (2021). Gellan gum. In *Handbook of Hydrocolloids* (pp. 855–885). Elsevier. https://doi.org/10.1016/B978-0-12-820104-6.00009-7

Tas, O., Ertugrul, U., Grunin, L., & Oztop, M. H. (2022). Investigation of the Hydration Behavior of Different Sugars by Time Domain-NMR. *Foods*, *11*(8), 1148. https://doi.org/10.3390/foods11081148

Tozzi, E. J., McCarthy, M. J., Lavenson, D. M., Cardona, M., Powell, and R. L., Karuna, N., & Jeoh, T. (2014). Effect of fiber structure on yield stress during enzymatic conversion of cellulose. *AIChE Journal*, *60*(5), 1582–1590. https://doi.org/10.1002/aic.14374

Uludag, Y., McCarthy, M. J., Barrall, G. A., & Powell, R. L. (2001). Polymer Melt Rheology by Magnetic Resonance Imaging. *Macromolecules*, *34*(16), 5520–5524. https://doi.org/10.1021/ma001543w

Westbrook, C., & Talbot, J. (2018). *MRI in Practice* (5th ed.). Wiley.

White, F. M. (1991). *Viscous fluid flow*. McGraw-Hill.

Wichchukit, S., McCarthy, M. J., & McCarthy, K. L. (2006). Flow Behavior of Milk Chocolate Melt and the Application to Coating Flow. *Journal of Food*

Science, *70*(3), E165–E171. https://doi.org/10.1111/j.1365-2621.2005.tb07131.x

Winkler, S. A., Schmitt, F., Landes, H., de Bever, J., Wade, T., Alejski, A., & Rutt, B. K. (2018). Gradient and shim technologies for ultra high field MRI. *NeuroImage*, *168*, 59–70. https://doi.org/10.1016/j.neuroimage.2016.11.033

Xia, Y., & Callaghan, P. T. (1991). Study of shear thinning in high polymer solution using dynamic NMR microscopy. *Macromolecules*, *24*(17), 4777–4786. https://doi.org/10.1021/ma00017a008

Yoon, W. B., & McCarthy, K. L. (2002). Rheology of yogurt during pipe flow as characterized by magnetic resonance imaging. *Journal of Texture Studies*, *33*(5), 431–444. https://doi.org/10.1111/j.1745-4603.2002.tb01358.x

APPENDICES

A. Statistical Analysis (ANOVA)

Table A.1. ANOVA Tables for the 'K' and 'n' values of Whole Milk and Almond Milk solutions – Conventional Rheometer

WORKSHEET 1

General Linear Model: K versus Samples

Method

Factor coding (-1, 0, +1)

Factor Information

Factor	Type	Levels	Values
Samples	Fixed	2	ALM, WM

Analysis of Variance

Source	DF	Adj SS	Adj MS	F-Value	P-Value
Samples	1	0.002335	0.002335	16695.52	0.000
Error	17	0.000002	0.000000		
Total	18	0.002337			

Model Summary

S	R-sq	R-sq(adj)	R-sq(pred)
0.0003740	99.90%	99.89%	99.87%

Coefficients

Term	Coef	SE Coef	T-Value	P-Value	VIF
Constant	0.014321	0.000086	166.69	0.000	
Samples					
ALM	0.011101	0.000086	129.21	0.000	1.00

Regression Equation

K = 0.014321 + 0.011101 Samples_ALM - 0.011101 Samples_WM

Comparisons for K

Tukey Pairwise Comparisons: Samples

Grouping Information Using the Tukey Method and 95% Confidence

Samples	N	Mean	Grouping
ALM	9	0.0254222	A
WM	10	0.0032200	B

Means that do not share a letter are significantly different.

General Linear Model: n versus Samples

Method

Factor coding (-1, 0, +1)

Factor Information

Factor	Type	Levels	Values
Samples	Fixed	2	ALM, WM

Analysis of Variance

Source	DF	Adj SS	Adj MS	F-Value	P-Value
Samples	1	0.262684	0.262684	12034.50	0.000
Error	17	0.000371	0.000022		
Total	18	0.263055			

Model Summary

S	R-sq	R-sq(adj)	R-sq(pred)
0.0046720	99.86%	99.85%	99.82%

Coefficients

Term	Coef	SE Coef	T-Value	P-Value	VIF
Constant	0.90115	0.00107	839.59	0.000	
Samples					
ALM	-0.11775	0.00107	-109.70	0.000	1.00

Regression Equation

n = 0.90115 - 0.11775 Samples_ALM + 0.11775 Samples_WM

Fits and Diagnostics for Unusual Observations

Obs	n	Fit	Resid	Std Resid	
1	1.00970	1.01889	-0.00919	-2.07	R

R Large residual

Comparisons for n

Tukey Pairwise Comparisons: Samples

Grouping Information Using the Tukey Method and 95% Confidence

Samples	N	Mean	Grouping
WM	10	1.01889	A
ALM	9	0.78340	B

Means that do not share a letter are significantly different.

Table A.2. ANOVA Tables for the 'K' values of methylcellulose solutions – Conventional Rheometer

General Linear Model: K versus Concentration

Method

Factor coding (-1, 0, +1)

Factor Information

Factor	Type	Levels	Values
Concentration	Fixed	4	MC_0.1, MC_0.5, MC_1, MC_2

Analysis of Variance

Source	DF	Adj SS	Adj MS	F-Value	P-Value
Concentration	3	1.11022	0.370072	3334.52	0.000
Error	8	0.00089	0.000111		
Total	11	1.11110			

Comparisons for K

Tukey Pairwise Comparisons: Concentration

Grouping Information Using the Tukey Method and 95% Confidence

Concentration	N	Mean	Grouping
MC_0.1	3	1.67114	A
MC_0.5	3	1.39882	B
MC_1	3	1.12714	C
MC_2	3	0.85485	D

Means that do not share a letter are significantly different.

Notes

Original K values did not satisfy the normality of the residuals. That is why Box-Cox transformation was applied to the data set. Box-Cox transformation yielded a value **'-0.1'.** Reported ANOVA values belong the data of $K^{-0.1}$**.**

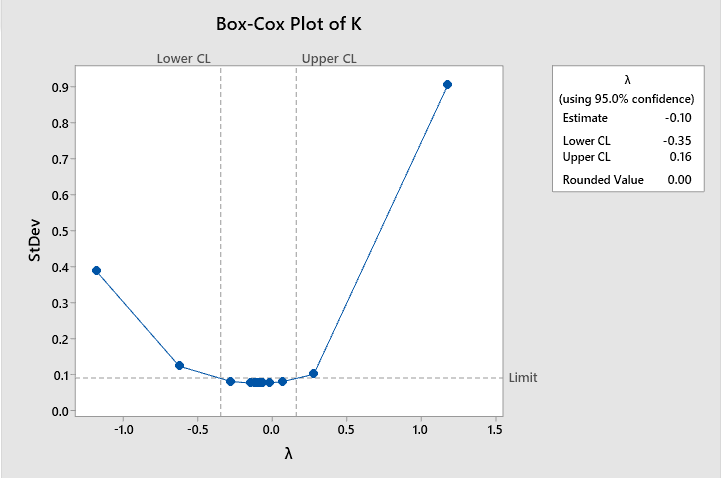

Table A.3. ANOVA Tables for the 'n' values of methylcellulose solutions-Conventional Rheometer

General Linear Model: n versus Concentration

Method

Factor coding (-1, 0, +1)

Factor Information

Factor	Type	Levels	Values
Concentration	Fixed	4	MC_0.1, MC_0.5, MC_1, MC_2

Analysis of Variance

Source	DF	Adj SS	Adj MS	F-Value	P-Value
Concentration	3	0.167667	0.055889	394.51	0.000
Error	8	0.001133	0.000142		
Total	11	0.168800			

Comparisons for n

Tukey Pairwise Comparisons: Concentration

Grouping Information Using the Tukey Method and 95% Confidence

Concentration	N	Mean	Grouping
MC_0.5	3	0.910000	A
MC_0.1	3	0.853333	B
MC_1	3	0.800000	C
MC_2	3	0.596667	D

Means that do not share a letter are significantly different.

Table A.4. ANOVA Tables for the 'K' values of methylcellulose solutions- Flow MR system

General Linear Model: K versus Sample

Method

Factor coding (-1, 0, +1)
Rows unused 2

Factor Information

Factor	Type	Levels	Values
Sample	Fixed	4	0.1-MC, 0.5-MC, 1-MC, 2-MC

Analysis of Variance

Source	DF	Adj SS	Adj MS	F-Value	P-Value
Sample	3	46.0019	15.3340	115.25	0.000
Error	5	0.6652	0.1330		
Total	8	46.6671			

Tukey Pairwise Comparisons: Sample

Grouping Information Using the Tukey Method and 95% Confidence

Sample	N	Mean	Grouping
0.1-MC	2	6.66817	A
0.5-MC	2	3.06939	B
1-MC	3	1.75223	C
2-MC	2	0.28613	D

Means that do not share a letter are significantly different.

Notes

Original K values did not satisfy the normality of the residuals. That is why Box-Cox transformation was applied to the data set. Box-Cox transformation yielded a value **'-1.40'.** Reported ANOVA values belong the data of $K^{-1.40}$**.**

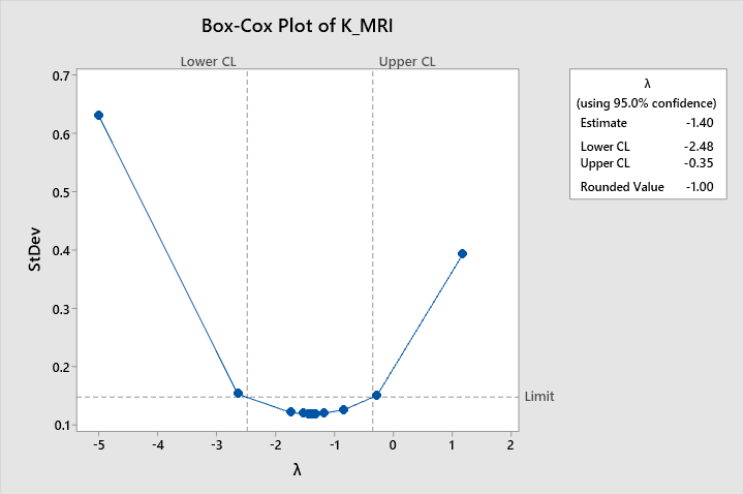

Table A.5. ANOVA Tables for the 'n' values of methylcellulose solutions- Flow MR system

General Linear Model: n_MRI versus Sample

Method

Factor coding (-1, 0, +1)
Rows unused 2

Factor Information

Factor	Type	Levels	Values
Sample	Fixed	4	0.1-MC, 0.5-MC, 1-MC, 2-MC

Analysis of Variance

Source	DF	Adj SS	Adj MS	F-Value	P-Value
Sample	3	0.035944	0.011981	197.60	0.000
Error	5	0.000303	0.000061		
Total	8	0.036247			

Comparisons for n_MRI

Tukey Pairwise Comparisons: Sample

Grouping Information Using the Tukey Method and 95% Confidence

Sample	N	Mean	Grouping		
0.1-MC	2	-0.036238	A		
1-MC	3	-0.047411	A		
0.5-MC	2	-0.075751		B	
2-MC	2	-0.200714			C

Means that do not share a letter are significantly different.

Notes

Original n values did not satisfy the normality of the residuals. That is why log transformation was applied to the data set.

Table A.6. ANOVA Tables for the comparison of 'n' values of methylcellulose solutions by Conventional and Flow MR systems

General Linear Model: Flow Behaviour Index versus Measurement Method, Sample Name

Method

Factor coding (-1, 0, +1)
Rows unused 4

Factor Information

Factor	Type	Levels	Values
Measurement Method	Fixed	2	CR, MRI
Sample Name	Fixed	4	0.1-MC, 0.5-MC, 1-MC, 2-MC

Analysis of Variance

Source	DF	Adj SS	Adj MS	F-Value	P-Value
Measurement Method	1	0.006422	0.006422	4.34	**0.058**
Sample Name	3	0.207319	0.069106	46.70	0.000
Error	13	0.019236	0.001480		
Lack-of-Fit	3	0.017319	0.005773	30.12	0.000
Pure Error	10	0.001917	0.000192		
Total	17	0.232978			

Table A.7. ANOVA Tables for the T_1 values of MC solutions

General Linear Model: T_1 versus Samples

Method

Factor coding (-1, 0, +1)

Factor Information

Factor	Type	Levels	Values
Samples	Fixed	4	0.1-MC, 0.5-MC, 1-MC, 2-MC

Analysis of Variance

Source	DF	Adj SS	Adj MS	F-Value	P-Value
Samples	3	235451	78484	62.33	0.000
Error	8	10074	1259		
Total	11	245525			

Comparisons for T_1

Tukey Pairwise Comparisons: Samples

Grouping Information Using the Tukey Method and 95% Confidence

Samples	N	Mean	Grouping		
0.1-MC	3	2890.50	A		
0.5-MC	3	2795.60		B	
1-MC	3	2722.97		B	
2-MC	3	2510.07			C

Means that do not share a letter are significantly different.

Table A.8. ANOVA Tables for the T_2 values of MC solutions

General Linear Model: T_2 versus Samples

Method

Factor coding (-1, 0, +1)

Factor Information

Factor	Type	Levels	Values
Samples	Fixed	4	0.1-MC, 0.5-MC, 1-MC, 2-MC

Analysis of Variance

Source	DF	Adj SS	Adj MS	F-Value	P-Value
Samples	3	2472205	824068	1580.13	0.000
Error	8	4172	522		
Total	11	2476377			

Comparisons for T_2

Tukey Pairwise Comparisons: Samples

Grouping Information Using the Tukey Method and 95% Confidence

Samples	N	Mean	Grouping
0.1-MC	3	2402.30	A
0.5-MC	3	2093.79	B
1-MC	3	1727.03	C
2-MC	3	1183.30	D

Means that do not share a letter are significantly different.

Table A.9. ANOVA Tables for the D values of MC solutions

General Linear Model: D versus Samples

Method

Factor coding (-1, 0, +1)

Factor Information

Factor	Type	Levels	Values
Samples	Fixed	4	0.1-MC, 0.5-MC, 1-MC, 2-MC

Analysis of Variance

Source	DF	Adj SS	Adj MS	F-Value	P-Value
Samples	3	0.050206	0.016735	62.43	0.000
Error	8	0.002145	0.000268		
Total	11	0.052351			

Comparisons for D

Tukey Pairwise Comparisons: Samples

Grouping Information Using the Tukey Method and 95% Confidence

Samples	N	Mean	Grouping
0.1-MC	3	2.49900	A
0.5-MC	3	2.43667	B

1-MC	3	2.42400	B	
2-MC	3	2.31900		C

Means that do not share a letter are significantly different.

Table A.10. ANOVA Tables for the T_1 values of milk samples

General Linear Model: T_1 versus Samples

Method

Factor coding (-1, 0, +1)

Factor Information

Factor	Type	Levels	Values
Samples_1	Fixed	2	ALM, WM

Analysis of Variance

Source	DF	Adj SS	Adj MS	F-Value	P-Value
Samples_1	1	6900.8	6900.83	94.09	0.002
Error	3	220.0	73.34		
Total	4	7120.9			

Comparisons for T_1

Tukey Pairwise Comparisons: Samples

Grouping Information Using the Tukey Method and 95% Confidence

Samples_1	N	Mean	Grouping
ALM	2	1623.20	A
WM	3	1547.37	B

Means that do not share a letter are significantly different.

Table A.11. ANOVA Tables for the T_2 values of milk samples

General Linear Model: T_2 versus Samples

Method

Factor coding (-1, 0, +1)

Factor Information

Factor	Type	Levels	Values
Samples_1	Fixed	2	ALM, WM

Analysis of Variance

Source	DF	Adj SS	Adj MS	F-Value	P-Value
Samples_1	1	162170	162170	22142.66	0.000
Error	3	22	7		
Total	4	162192			

Comparisons for T_2

Tukey Pairwise Comparisons: Samples

Grouping Information Using the Tukey Method and 95% Confidence

Samples_1	N	Mean	Grouping
ALM	2	551.650	A
WM	3	184.033	B

Means that do not share a letter are significantly different.

Table A.12. ANOVA Tables for the D values of milk samples

General Linear Model: D versus Samples

Method

Factor coding (-1, 0, +1)

Factor Information

Factor	Type	Levels	Values
Samples_1	Fixed	2	ALM, WM

Analysis of Variance

Source	DF	Adj SS	Adj MS	F-Value	P-Value
Samples_1	1	0.175109	0.175109	70.01	0.004
Error	3	0.007504	0.002501		
Total	4	0.182613			

Tukey Pairwise Comparisons: Samples

Grouping Information Using the Tukey Method and 95% Confidence

Samples_1	N	Mean	Grouping
ALM	2	2.302	A
WM	3	1.920	B

Means that do not share a letter are significantly different.

B. MATLAB Codes

B.1. Flow MRI Rheology Calculator

Open MATLAB code below is written to calculate the shear rate and shear stress from velocity image and additional parameters: *radial position, velocity profile, pressure difference, distance between pressure transducers, radius of pipe, density of sample to analyze*. It performs the necessary fitting to obtain Power law model parameters, n and K.

```
%% MRI Rheology parameter calculator
%Inputs: radial position,velocity profile, and pressure differance
%constants: distance,(l), between pressure transducers, radious of pipe
and
%and parameters to calculate static pressure p*g*l
%outputs:Power law parameters n and K

%% INPUTS
R = input("Radial position matrix (horizontal vector matrix):");
v = input("Velocity profile(horizontal vector matrix):");
DP = input("Pressure differance (Pa):");
l = input("Distance between pressure transducers(m):");
p = input("Density of the sample (kg/m^3):");
g = 9.80665;

%% Velocity to Shear rate calculations
% Velocity:v
% Radious: R
x=[ones(size(R')) R' R'.^2 R'.^3 R'.^4];

v=v';
prmtrs=x\v;
Vcal = x*prmtrs;
prmtrs = prmtrs';



%% Calculate shear rates using the first derivatavation
velocity = -(4*prmtrs(1,5)*abs(R).^3+3*prmtrs(1,4)*abs(R).^2 +
2*prmtrs(1,3)*abs(R) + prmtrs(1,2)*abs(R));
shearrate    = -(4*3*prmtrs(1,5)*abs(R).^3 + 3*prmtrs(1,4)*abs(R).^2 +
2*prmtrs(1,3)*abs(R)); % first derivatives of velocity according to r
direction
```

```
%% Shear stress
static_DP=l*g*p;
DP=DP-static_DP;
sstress = abs(R)*(max(R))*DP./(2*l); % l: length between pressure
transducers, DP: Pressure differance



%% Power law model fit y = ax + b

x=log(shearrate);
y=log(sstress);

[c,st]=polyfit(x,y,1);    % y = (c1)*x + (c2)

n = c(1,1);               % flow behavior index
K = exp(c(1,2));          % Consistency index

[yfit, delta]=polyval(c,x,st);

ndata = length(x);
sx=sum(x);
sxx=sum(x.^2);
sy=sum(y);
xbar=sx/ndata;
ybar=sy/ndata;

sxy=sum((x-xbar).*(y-ybar));
ssx=sum((x-xbar).^2);      %% sum of sqaures in x
sse=sum((y-yfit).^2);      %% sum of squares due to error
ssr=sum((yfit-ybar).^2);   %% sum of squares of the regression
sst=sum((y-ybar).^2);      %% total sum of squares

r2=ssr/sst;     %% R square

plot(shearrate,sstress);

xlabel("Shear Rate (1/s)");
ylabel("Shear Stress (Pa)");

str = {"n=" + n "K=" + K  "r2=" + r2};
a = median(sstress);
text(15,a,str);
```

B.2. Pressure Sensor Data Acquisition MATLAB

The open MATLAB code that is displayed below is created to convert two pressure sensors signal to pressure reading in the flow system.

```
numReadings = 10;
delay = 2;
% Make the LJM .NET assembly visible in MATLAB
ljmAsm = NET.addAssembly('LabJack.LJM');
% Creating an object to nested class LabJack.LJM.CONSTANTS
t = ljmAsm.AssemblyHandle.GetType('LabJack.LJM+CONSTANTS');
LJM_CONSTANTS = System.Activator.CreateInstance(t);
handle = 0;
% T7 device, Any connection, Any identifier
[ljmError, handle] = LabJack.LJM.OpenS('T7', 'ANY', 'ANY', handle);
% Any device, Any connection, Any identifier
% [ljmError, handle] = LabJack.LJM.Open(LJM_CONSTANTS.dtANY, ...
% LJM_CONSTANTS.ctANY, 'ANY', handle);
% showDeviceInfo(handle)
% Setup and call eWriteNames to configure
% LabJack T7
% AIN0 and AIN1:
% Negative Channel = 1
% Range = +/-0.1 V
% Resolution index = 0 (default)
% Settling = 50000
numFrames = 28;
aNames = NET.createArray('System.String', numFrames);
aNames(1) = 'AIN0_EF_INDEX';
aNames(2) = 'AIN0_EF_CONFIG_A';
aNames(3) = 'AIN0_EF_CONFIG_D';
aNames(4) = 'AIN0_EF_CONFIG_E';
aNames(5) = 'AIN0_EF_CONFIG_C';
aNames(6) = 'AIN0_NEGATIVE_CH';
aNames(7) = 'AIN0_RANGE';
aNames(8) = 'AIN0_RESOLUTION_INDEX';
aNames(9) = 'AIN0_SETTLING_US';
aNames(10) = 'AIN1_RANGE';
aNames(11) = 'AIN1_RESOLUTION_INDEX';
aNames(12) = 'AIN2_EF_INDEX';
aNames(13) = 'AIN2_EF_CONFIG_A';
aNames(14) = 'AIN2_EF_CONFIG_D';
aNames(15) = 'AIN2_EF_CONFIG_E';
aNames(16) = 'AIN2_EF_CONFIG_C';
aNames(17) = 'AIN2_NEGATIVE_CH';
aNames(18) = 'AIN2_RANGE';
aNames(19) = 'AIN2_RESOLUTION_INDEX';
aNames(20) = 'AIN2_SETTLING_US';
aNames(21) = 'AIN3_RANGE';
aNames(22) = 'AIN3_RESOLUTION_INDEX';
aNames(23) = 'AIN12_RANGE';
aNames(24) = 'AIN12_RESOLUTION_INDEX';
aNames(25) = 'AIN12_SETTLING_US';
aNames(26) = 'AIN13_RANGE';
aNames(27) = 'AIN13_RESOLUTION_INDEX';
aNames(28) = 'AIN13_SETTLING_US';
aValues = NET.createArray('System.Double', numFrames);
aValues(1) = 24;
```

```
aValues(2) = 1;
aValues(3) = 1.0;
aValues(4) = 0.0;
aValues(5) = 60052;
aValues(6) = 1;
aValues(7) = 10; % range by_ziko
aValues(8) = 0;
aValues(9) = 50000;
aValues(10) = 10; % range by_ziko
aValues(11) = 0;
aValues(12) = 24;
aValues(13) = 1;
aValues(14) = 1.0;
aValues(15) = 0.0;
aValues(16) = 60052;
aValues(17) = 3;
aValues(18) = 0.1;
aValues(19) = 0;
aValues(20) = 50000;
aValues(21) = 0.1;
aValues(22) = 0;
aValues(23) = 10;
aValues(24) = 16;
aValues(25) = 50000;
aValues(26) = 10;
aValues(27) = 16;
aValues(28) = 50000;
% end
LabJack.LJM.eWriteNames(handle, numFrames, aNames, aValues, 0);
% Setup and call eReadNames to read AINs.
numFrames = 4;
aNames = NET.createArray('System.String', numFrames);
aNames(1) = 'AIN0_EF_READ_A';
aNames(2) = 'AIN2_EF_READ_A';
aNames(3) = 'AIN0'; % by_ziko
aNames(4) = 'AIN1'; % by_ziko
aValues = NET.createArray('System.Double', numFrames);
% numReadings = 10
% delay = 1; % Delay (in sec.) between readings
% disp(['Performing ' num2str(numReadings) ' AIN0 EF, AIN2 EF, AIN12 and
AIN13 readings ' ...
% 'with ' num2str(delay) ' second delay between readings:']);
lowerpressuretransducer = zeros(numReadings,1);
upperpressuretransducer = zeros(numReadings,1);
for i = 1:numReadings
LabJack.LJM.eReadNames(handle, numFrames, aNames, aValues, 0);
% disp([' ' char(aNames(1)) ': ' num2str(aValues(1)) ' F, ' ...
% char(aNames(2)) ': ' num2str(aValues(2)) ' F, ' ...
% char(aNames(3)) ': ' num2str(aValues(3)) ' V, ' ...
% char(aNames(4)) ': ' num2str(aValues(4)) ' V'])
lowerpressuretransducer(i) = aValues(3);
upperpressuretransducer(i) = aValues(4);
pause(delay);
```

```
end
% pressures in Pa
% lowerpressuretransducer & upperpressuretransducer in unit Volt
pressures(:,1) = lowerpressuretransducer*0.25*10^5; % by_ziko
%pressures(:,1) = 100.*(8.475.*lowerpressuretransducer-4.0)./16.0;
%upstream pressure = lower pressure transducer
%pressures(:,2) = Plower_PSI*6894.76;
pressures(:,2) = upperpressuretransducer*0.25*10^5; % by_ziko
%downstream pressure = upper pressure transducer
%pressures.Pupper_Pa = Pupper_PSI*6894.75;
display(mean(pressures
```